

1 **Fifty-year seasonal variability of East African droughts and floods recorded in Central**
2 **Afar lake sediments (Ethiopia) and their connections with ENSO**

3
4 Carlo Mologni ^{1*}, Marie Revel ¹, Eric Chaumillon ², Emmanuel Malet ³, Thibault Coulombier
5 ², Pierre Sabatier ³, Pierre Brigode ¹, Gwenael Hervé ⁴, Anne-Lise Develle ³, Laure Schenini ¹,
6 Medhi Messous ¹, Gourguen Davtian ⁶, Alain Carré, ⁶, Delphine Bosch ⁷, Natacha Volto ²,
7 Clément Ménard ⁵, Lamy Khalidi ⁶, Fabien Arnaud ³

8
9 ¹ Université Côte d'Azur, CNRS, OCA, IRD, Geoazur, 250 rue Albert Einstein, 06500 Valbonne,
10 France.

11 ² University of La Rochelle, UMR CNRS 7266 LIENSs, La Rochelle, France.

12 ³ Environnement Dynamique et Territoire de Montagne (EDYTEM), CNRS, Université Savoie Mont-
13 Blanc, Le Bourget du lac, France.

14 ⁴ Laboratoire des Sciences du Climat et de l'Environnement/IPSL, CEA, CNRS, UVSQ, University of
15 Paris-Saclay, Gif-sur-Yvette, France.

16 ⁵ EPCC, Centre Européen de Préhistoire, Avenue Léon-Jean Grégory - 66720 – Tautavel, France

17 ⁶ Université Côte d'Azur, CNRS, CEPAM – UMR 7264, 24 av. des Diabes Bleus 06300 Nice, France.

18 ⁷ Géosciences Montpellier, UMR-CNRS 5243, Université de Montpellier, 34095 Montpellier, France

19 *Corresponding author
20

21 **Abstract**

22 Understanding past and present hydro-system feedbacks to global ocean-atmospheric interactions
23 represents one of the main challenges to preventing droughts, extreme events and related human
24 catastrophes in the face of global warming, especially in arid and semiarid environments. In eastern
25 Africa, the El Niño-Southern Oscillation (ENSO) was identified as one of the primary drivers of
26 precipitation variability affecting water availability. However, the northern East African Rift System
27 (EARS) still suffers from the underrepresentation of predictive and ENSO teleconnection models
28 because of the scarcity of local-to-regional historical or palaeo-data.

29 In this paper, we provide a 50-year seasonal flood/drought chronicle of the Awash River catchment from
30 the study of laminated sediment from Gemeri and Afambo lakes (Central Afar region, Ethiopia), with
31 the aim of reconstructing the magnitude of regional hydro-climatic events. Pluri-centimetric micro-
32 laminated lithogenic facies alternating with pluri-millimetric carbonate-enriched facies are investigated
33 in both lakes. We couple dating methods including radiocarbon, short-lived radionuclides,
34 palaeomagnetic field variations and varve counting on both lake deposits to build a high-resolution age
35 model and to discuss the regional hydro-sedimentary dynamics of the Awash River over the last ~700
36 years, with a focus on the last fifty years.

37 Using a multiproxy approach, we observe that following a multi-centennial enhanced hydrological
38 period, the two lakes experienced a gradual decrease in river load inflow since 1979 CE, attaining
39 extreme drought and high evaporative conditions between 1991 and 1997 CE. In 2014, the construction
40 of a dam and the improvement of agricultural water management in the lower Awash River plain
41 impacted the erodibility of local soils and the hydro-sedimentary balance of the lake basins, as evidenced
42 by a disproportionate sediment accumulation rate.

43 Comparison of our quantitative reconstruction with i) lake water surface evolution, ii) the interannual
44 Awash River flow rates, and iii) the El Niño 3.4 model highlights the intermittent connections between
45 ENSO Sea Surface Temperature anomalies, regional droughts and hydrological conditions in the
46 northern EARS.

47 **1 Introduction**

48 According to the Sixth Assessment Report of the Intergovernmental Panel on Climate Change (IPCC),
49 climate warming has been more rapid in Africa in recent decades than in any other region of the world
50 (IPCC, 2022). Between March and August across Eastern Africa, the monsoonal rainy season is vital
51 for agricultural production and thus for national food security, especially in more susceptible areas such
52 as along the Rift Valley and over distal lowlands. During the last ~50 years, recurrent reduced rainy
53 seasons have had substantial environmental, humanitarian and economic impacts, including agriculture
54 and ecosystem sustainability (Palmer et al., 2023). Global climate projections further suggest that the
55 Horn of Africa will experience strong disturbances of its usual hydrological cycle, with both increasing
56 frequency of intense rainfall events leading to enhanced flash-flood hazards and a generalized scarcity
57 of rainfall, leading to frequent severe drought episodes (Palmer et al., 2023). Such climatic instability
58 may induce the collapse of the local food production system, leading to famine, as it occurred in the
59 decades between 1970 and 1990 (FAO, 2000). More recently, the shorter-than-normal 2021 rainy season
60 led to a 70% reduction in average precipitation compared with seasonal norms, which raised an
61 international alert and mobilization for the mitigation of desertification processes in the Horn of Africa
62 (FAO, 2022).

63 Facing such evidence, eastern Africa is currently the focus for understanding recent (Late Holocene)
64 past climate dynamics (Lennard et al., 2018) to simulate future projections, support regional ecosystem
65 sustainability (Niang et al., 2014) and reduce rural population vulnerability to climate warming (FAO,
66 2022). Palaeoclimatic reconstructions have long been used to understand past climate variability to build
67 more robust future climatic models in Africa. Even if global climate and hydrological model simulations
68 have made considerable progress, reconstructions or tendencies of future precipitation and atmospheric
69 dynamics in eastern Africa which affect continental hydrology at the regional-to-local scale remain to
70 be developed (Dosio et al., 2019; Lennard et al., 2018). Indeed, the lack of widespread regional-to-local
71 palaeoclimatic data makes it difficult to establish regional climatic models and the link between global
72 hydroclimate variability and the functioning of specific hydro-systems.

73 In East Africa, precipitation variability is influenced by multiple interactions between patterns of remote
74 climate forcing, regional circulation and local geographic factors acting at local and global scales
75 (Nicholson, 2017). At a wider scale, the El Niño-Southern Oscillation (ENSO) was identified as one of
76 the primary drivers of precipitation in eastern Africa (Ficchi et al., 2021; Nicholson, 2017; Palmer et al.,
77 2023). More research on regional and high-temporal resolution relationships between ENSO and
78 flood/drought impacts in the present and in the past is increasingly needed (Ficchi et al., 2021; Ward et

79 al., 2014). With the aim of filling this gap, this paper focuses on the acquisition of new hydro-
80 sedimentary datasets (i.e., decennial to seasonal scale resolution) thanks to the study of lacustrine
81 sedimentary sequences from one of the wider river catchments in the northern East African Rift System
82 (EARS), namely the Awash River basin (Fig. 1).

83 As flood occurrence and magnitude of the Awash River are mainly linked to fluctuation of the Ethiopian
84 Highland precipitation regime over time, the establishment of regional flood chronicles from natural
85 archives is key to evaluating the evolution of precipitation variability on land (Ficchi et al., 2021;
86 Mologni et al., 2020; Wilhelm et al., 2022). Of all of the natural archives for hydrological reconstruction,
87 lakes are privileged because they act as natural sinks, continuously trapping erosion products from an
88 entire catchment over a long period (Sabatier et al., 2022; Wilhelm et al., 2018). Indeed, during flood
89 events, water-transported detrital particles (or sediment discharge) are deposited on the lake bottom in
90 the form of graded layers that differ from the intra-lake sedimentation related to lake productivity. Thus,
91 lake sedimentary deposits are valuable to fully understand the relationships between hydroclimate,
92 rainfall, floods, droughts and lake water conditions at the regional scale.

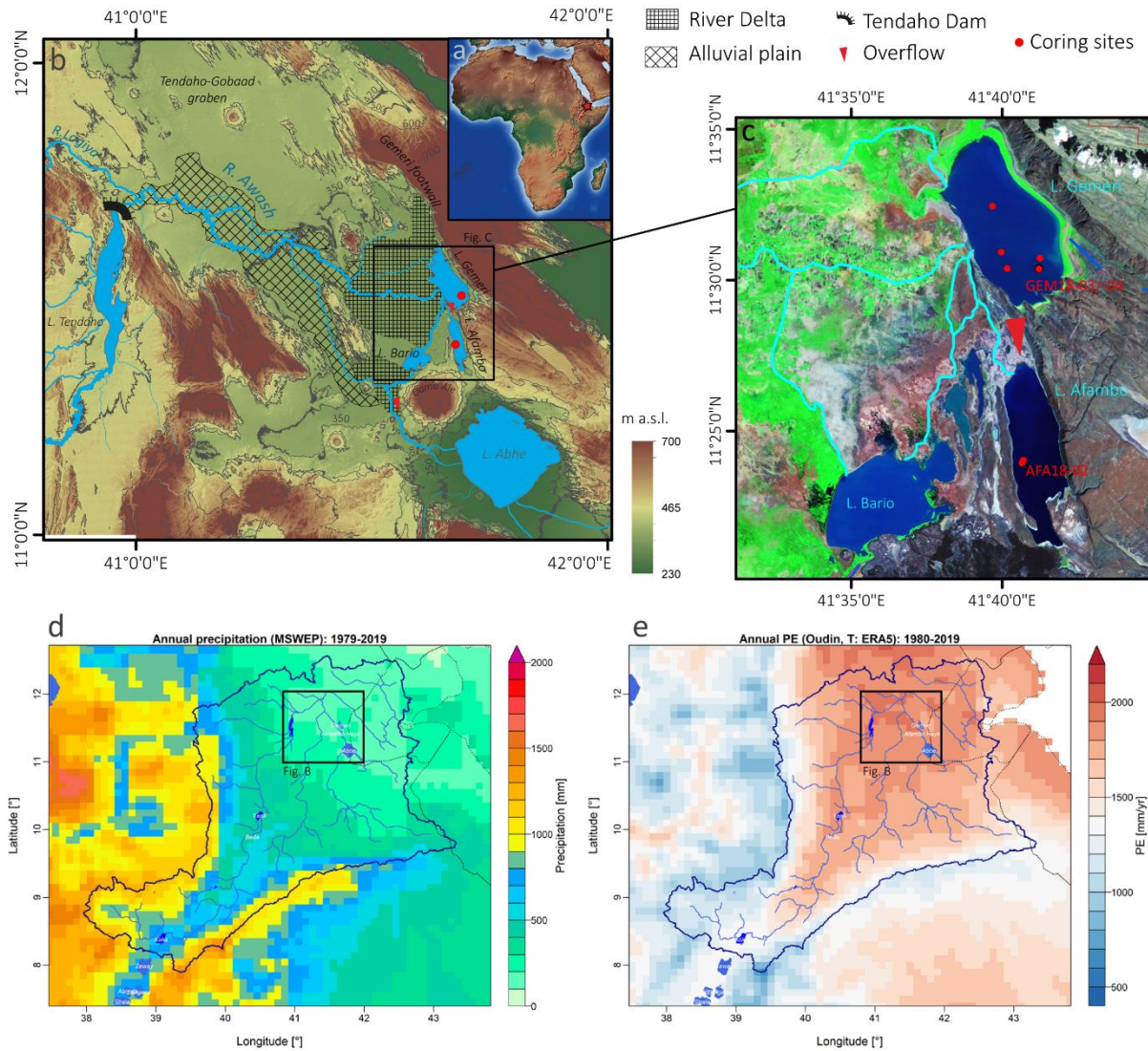
93 This paper presents the results from a multiproxy study combining a seismic survey with
94 sedimentological and geochemical analyses performed on archives from the Afambo and Gemeri lakes
95 located in the Abhe lake basin (Central Afar Region, Ethiopia, Fig. 1). The main objective of this study
96 is to quantify variations of long-term Awash River solid sedimentary discharges to establish regional
97 flood activity chronicle and to reconstitute the hydrological regime of the Awash River. We aim first to
98 identify the hydro-sedimentary processes in the Afambo and Gemeri Lake basins (Central Afar Region,
99 Ethiopia) under human and hydroclimate/meteorological forcing over the long-term. Finally, we
100 compare these flood and drought chronicles with global ENSO records and discuss the interaction
101 between atmospheric anomalies, droughts and hydrological conditions in the northern EARS.

102 **2 Study site: hydrological and geomorphological settings**

103 **2.1 Regional hydroclimatic patterns**

104 The Abhe Lake basin, located at the northern extremity of the EARS ($\sim 12^\circ$ N), is the widest and longest
105 rifting-controlled sedimentary basin of the Afar Rift System (Fig. 1a). It corresponds to the topographic
106 depression of the lower Awash valley (Fig. 1b) consisting of an area of 6 000 km² (Mologni et al., 2021).
107 The Central Afar Region is currently a desert receiving ~ 400 mm/yr of local precipitation (Fig. 1d) with
108 a mean annual evapotranspiration of ~ 2000 mm/yr (Fig. 1e). In such a dry context, the permanency of
109 waterbodies such as lakes Gemeri and Afambo (Fig. 1c) is mainly supported by their hydrological
110 dependence on permanent Awash River water supplies originating in the Ethiopian highlands (mean
111 annual precipitation ~ 1000 mm/yr; Fig. 1d), whereby the hydrological regime is dominated by seasonal
112 rainfall pertaining to the southwest African monsoon. With a drainage basin surface of over 112,700

113 km², the Awash River has an annual runoff of 4.6 BM³. However, 72% of it is lost to evapotranspiration
 114 in the lowlands (Taddese et al., 2010).
 115



116
 117 **Figure 1:** Geographical, geomorphological and hydrological contexts of the study area and coring sites. **A)** Location of the
 118 Central Afar Region on a topographic map of Africa (red star, ESRI database); **B)** Digital Elevation Model of the Lake Abhe
 119 basin (SRTM) corresponding to the Lower Awash Valley with the location of Gemberi, Afambo and Abhe waterbodies, the
 120 corresponding alluvial plain and the Awash River delta, the main coring sites (red dots), the overflow directions and the
 121 Tendaho dam; **C)** Focus on Lakes Afambo and Gemberi study sites with the location of coring sites (red dots), the local
 122 hydrographic network (light blue lines) and the overflow direction between the waterbodies; **D)** mean annual precipitation
 123 over the Awash River and Lake Abhe basins estimated over the 1979-2019 period using the MSWEP dataset Beck et al. (2019).
 124 **E)** Mean annual potential evapotranspiration over the Awash River and Lake Abhe basins estimated using the Oudin et al.
 125 (2005) formula and the air temperature of the ERA5 dataset Hersbach et al. (2020).

126 When it feeds into Lakes Gemberi and Afambo Lakes, the Awash River has only crossed recent
 127 geological formations subsequent to the formation of the Oligocene Ethiopian basaltic trap flows. The
 128 lower Awash Valley is mainly composed of stratoid basalts formed between 4 and 0.4 Ma (Awaleh et
 129 al., 2016, Barberi and Varet, 1977; Varet, 2018) and intra-graben Quaternary accumulations, which still
 130 belong mainly to the Stratoid series group.

131 **2.2 Local geomorphological context**

132 The northern part of the Lake Abhe basin is composed of an alluvial plain corresponding to irrigated
133 agricultural fields and extended anthropogenic water channels, and a lobate delta in its lower part (Fig.
134 1b). The remaining edges of the basin are composed of desert plains and basaltic/rhyolitic outcrops that
135 constitute the Tendaho-Gobaad graben horsts (Fig. 1b). The delta fan spreads ~60 km from the northern
136 Gemeri footwall fault through the Gemeri and Bario waterbodies until the Dama Ale volcano slopes to
137 the south (Fig. 1b).

138 The Awash freshwater supplies first reach Lake Gemeri (11°51'N, 41°69' E), and overflowing into Lake
139 Afambo (11° 40' N, 41° 68' E). In contrast to Gemeri, Lake Afambo is not located on the delta fan and
140 does not possess any aerial estuary (Fig. 1b, c). Indeed, Afambo Lake is reached during the dry season
141 by a single water channel and is permanently separated from the deltaic swamps by north-south basaltic
142 outcrops (Fig. 1c, 2a). The rest of the Awash water supply is drained by the delta to the Bario waterbody
143 and to the terminal river channel that flows down to Lake Abhe (Fig. 1b, c).

144 The local hydrological network led us to select two complementary coring sites for this study: Lake
145 Gemeri, which borders the prodeltaic zone, mostly records the sedimentary signal from fluvial dynamics
146 (Awash River solid load), and Lake Afambo, which is partially disconnected from deltaic dynamics, has
147 the potential to record fine-grained sediment inputs, lacustrine primary productivity processes and to
148 preserve the sedimentary record from hiatuses due to deltaic erosional dynamics.

149 The hydrological network of the Lower Awash River plain has been modified by the building of a dam
150 for the agricultural development of this area conducted by the "*Tendaho Dam and Irrigation Project*"
151 (Dereje et al., 2018; Kidane et al., 2014). The dam is located upon entry of the Awash River waters into
152 the Lake Abhe basin area (Fig. 1b). The construction project began in 2010, and the dam started working
153 in early 2014. Such massive infrastructure has led to the formation of the Tendaho artificial lake (Fig.
154 1b) and the current network of irrigation channels in the alluvial plain.

155 **3 Materials and methods**

156 **3.1 Analysis of the water surface evolution of Lake Gemeri from satellite** 157 **images (1984 – 2019)**

158 We conducted imagery analyses of the water surfaces of Lakes Gemeri and Afambo from 1984 to 2021.
159 We used the "Global Surface Water" dataset from the Copernicus Programme, which was generated
160 using 4,716,475 montly and sub-montly scenes from Landsat 5, 7, and 8 acquired between March 1984
161 and December 2021 by Landsat satellites provided by the USGS and NASA. The dataset contains maps
162 of the location and temporal distribution of surface water from 1984 to 2021 at 30 m resolution and
163 provides statistics on the extent and change of those water surfaces. For more information, refer to the

164 associated journal article by Pekel et al. (2016). From this dataset, we computed statistics about the
165 extent and change of the water surfaces. Using Envi software, version 5.4, we created a Meta image
166 with the 37 water surface maps from 1985 to 2021 and generated statistics for the Meta image, which
167 were then exported.

168 However, for the years 1988, 1989, 1990, 1992, 1993, 1996, and 1997, the “Global Surface Water”
169 dataset algorithm failed to concretely calculate the water surfaces, resulting in imprecise or missing data.
170 As a result, we employed the quality assessment (QA) band in Landsat 5 images, which provides
171 information on features such as clouds, shadows, ice, bare land, and water. Classification
172 algorithms were applied to assign binary values to bits in the QA band based on pixel characteristics.
173 By importing archives from the USGS and utilizing the Pixel_QA band associated with the available
174 images, a water mask was created. This water mask allowed us to perform zonal statistics using ArcGIS
175 Pro 3.0.3.

176 **3.2 Seismic survey**

177 In December 2018, a seismic reflection survey was conducted in the southernmost part of Lake Gemeri
178 with the aim of exploring the internal architecture of the lake sedimentary fill and choosing the location
179 of the coring site. The acquisition of 12 seismic profiles of Lake Gemeri (Fig. S1, S2) was performed
180 using an IxBlue ECHOES 5000 CHIRP echo-sounder (LIENSs laboratory, La Rochelle, France). Chirp
181 frequency band 2000 - 8000 Hz was selected, with a chirp length of 50 ms. Chirp data processing
182 included auto grain control, time varying gain, staking of adjacent traces, and swell filtering.

183 **3.3 Coring of Gemeri and Afambo Lakes**

184 In December 2018, 10 short sedimentary cores were retrieved from Lakes Gemeri and Afambo during
185 the CLIMAFAR 2018 survey. Shorter cores were retrieved using a UWITEC gravity corer, while a
186 homemade modified Nesje-like corer permitted us to reach slightly more than 2 m sediment depth in
187 Lake Gemeri (Fig. 1c). Details about the coring operations can be found on the French National
188 Cybercatheque (<https://cybercarotheque.fr/index.php?ope=530>).

189 We focused the present study on cores collected in the deepest part of each lake, i.e., GEM18-03 (length
190 144 cm, IGSN number TOAE0000000354) and GEM18-04 (209 cm, IGSN number:
191 TOAE0000000356) taken at 6 m water depth in Lake Gemeri, and AFA18-02 (173 cm, IGSN number
192 TOAE0000000348) taken in Lake Afambo at 18 m water depth. GEM18-04 was cut into two parts in
193 the field, and only the deepest part (109-209 cm below lake floor) of the overlapping core GEM18-03,
194 was studied here. Core sections were split length-wise, photographed at high resolution, and described
195 and logged in detail using the Munsell colour chart at the EDYTEM sedimentary lab facility. The
196 identification of specific layers on the overlapping sections GEM18-03 and GEM18-04B together with

197 the comparison of XRF core scanner and magnetic susceptibility signals led us to propose a 2.2 m long
198 composite sediment sequence from Lake Gemeri, hereafter called GEM18-03/04.

199 **3.4 Analytical methods**

200 **3.4.1 XRF core scanner on soft sediments, ICP–MS measurements and clay** 201 **mineralogy**

202 To characterize the variation in major elements throughout cores GEM18-03/04 and AFA18-02, we
203 performed non-destructive X-ray fluorescence (XRF) geochemical analyses on an AVAATECH Core
204 Scanner at the EDYTEM laboratory (CNRS-Université de Savoie Mont-Blanc, France). The XRF
205 analyses were performed following a 1 mm sampling step for the AFA18-02 section A, 2 mm for the
206 lower section B (live time = 20s), and 5 mm for the GEM18-03/04 core. At each step, two successive
207 measurements were performed at 10 kV (0.12mA) and 30 kV (0.15mA) voltages to assess the
208 contribution of lighter (Al, Si, S, K, Ca, Ti, Mn, Fe) and heavier (Br, Sr, Rb, Zr, Pb) elements,
209 respectively. Each individual power spectrum was transformed by deconvolution into relative contents
210 of each computed element expressed in counts per second (cps). XRF data were subsequently
211 transformed with a Centred Log-Ratio transformation package on R© software, with the aim of
212 circumventing problems associated with matrix effects (e.g., variable water content and grain-size
213 distribution) and irregularities of the core surface (Weltje and Tjallingii, 2008).

214 Principal component analysis (PCA) was performed on the XRF results using R© software (Sup. Mat.
215 S3) with the aim of characterizing the main geochemical signatures of particles composing the GEM18-
216 03/04 and AFA18-02 sediments.

217 Major and trace element analyses were performed with a Quadrupole ICP–MS (AETE-ISO platform,
218 Geosciences Montpellier, France) on 500 mg of powdered and homogenized sediment sample for 6
219 discrete samples in the GEM18-03/04 core and 11 discrete samples from the AFA18-02 core (Rauch et
220 al., 2006).

221 X-ray diffraction analyses on clay minerals were performed on 5 samples from the GEM18-03/-04
222 sequence at the LHyGS laboratory CNRS-UMR7517 (Strasbourg, France) (Sup. Mat. S6). Sediments
223 were treated with HCl (10%) solution to avoid any carbonate content. Suspended clay fractions were
224 separated following the procedure in Jackson (2005) and mounted on thin sections for oriented clay
225 XRD analyses. With the aim of acquiring the whole diffraction spectrum, four diffractograms were
226 obtained using a D8-Advance-Eco machine from the same sample with normal treatment, ethylene-
227 glycol treatment, hydrazine treatment, and heat treatment for 4 h at 490°C. The semiquantitative content
228 of clay minerals (%) was obtained from MacDiff version 4.1.2 software as a 2q° counts per second (cps)
229 spectrum area measurement.

230 **3.4.2 Sedimentological analyses**

231 Grain-size analyses were performed at the Geoazur laboratory using a Coulter-LS2000 with a size range
232 between 0.005 μm and 3775 μm . The analysis was performed following a 2.5 mm sampling step for the
233 AFA18-02 core. We determined the grain size of the intercepts for 10%, 50% and 90% of the cumulative
234 grain size curves (named D90, D50 and D10 values; Folk and Ward, 1957). We use the coarsest fraction
235 (D90) to characterize the deposit energy and to propose a hydrodynamic interpretation as suggested by
236 Wilhelm et al., (2018).

237 Optical microscopic analyses were focused on 8 thin sections (10 x 2 cm) sampled from the AFA18-02
238 sequence and processed at the litho-preparation facilities of the EDYTEM laboratory (Arnaud and
239 Sabatier, 2022). Microscopic observations were obtained on a Leica DM4 P at the Geoazur Laboratory
240 at 25x and 1000x magnification using plane-polarized (PPL), crossed-polarized (XPL) and oblique
241 incident (OIL) lights. Loss On Ignition (LOI) was performed on crushed sediment for each analysed
242 sample at the CEPAM-UMR7264 laboratory (Sup. Mat. S5). Samples were heated for 24 h at 100°C
243 with the aim to determine the residual water and gypsum content. Subsequently samples were heated
244 for 4 h at 550°C with the aim to determine total content measures of organic carbon (Santisteban et al.,
245 2004). LOI is expressed in percentage (%).

246

247 **3.4.3 Chronology of Gemer and Afambo Lake sequences**

248 On the GEM18-03/04 sediment sequence, we combined short-lived radionuclides (^{210}Pb and ^{137}Cs), ^{14}C
249 measurements and palaeomagnetic analyses to build a reliable age-depth model along the 2.2 m of the
250 composite section. A continuous sampling step of 6 cm was applied over the uppermost 66 cm of
251 GEM18 to determine ^{210}Pb and ^{137}Cs activities using well-type germanium detectors (SAGe Well)
252 located below 1700 m of rocks at the “laboratoire souterrain de Modane” (CNRS-Université Grenoble
253 Alpes) to reduce the influence of cosmic rays on gamma measurements (Reyss et al., 1995).
254 Radionuclide-based age models were computed using the *serac* R package (Bruel and Sabatier, 2020).
255 For the ^{210}Pb ex model, we choose the CFCS (Constant Flux Constant Sedimentation) model because
256 CRS (Constant Rate of Supply) cannot be applied in this context in regard to 1/ the hiatus (which affect
257 the ^{210}Pb ex inventory) and 2/ the age of the AFA core which not allow to estimate the total ^{210}Pb ex
258 inventory need for CRS model calculation. We not applied the CIC (Constant Initial Concentration)
259 model because it will result in age inversion in regard to ^{210}Pb ex fluctuation.

260 ^{14}C measurements were performed on 9 bulk organic matter and 4 shell samples (Fig. S23) using the
261 ARTEMIS accelerator mass spectrometry (AMS) facility at the LSCE-LMC14 laboratory (Gif-sur-
262 Yvette, France).

263 Palaeomagnetic measurements were performed on the entirety of the GEM18-03/-04 composite section.
264 The principle of the palaeomagnetic method is to compare the declination, inclination and relative
265 palaeointensity (RPI) records from the dated core with a reference curve of the secular variations in the

266 geomagnetic field (Crouzet et al., 2019; Haberzettl et al., 2019; Li et al., 2021; Ólafsdóttir et al., 2013).
267 Measurements were performed at the LSCE on u-channels sampled from the center of the GEM18-03
268 and GEM18-04B half cores. The direction of the characteristic remnant magnetization (ChRM),
269 assumed to be a detrital remnant magnetization (DRM) acquired during the deposition of the sediment,
270 was determined after alternating field (AF) demagnetization. The rock magnetic properties were
271 investigated on u-channels from measurements of low-field susceptibility, acquisition and
272 demagnetization of ARM and IRM, coupled to thermomagnetic, hysteresis curves and first order
273 reversal curves (FORC) on 9 discrete samples. The full protocol is detailed in the supplementary
274 material (Sup. Mat. S5).
275 The age depth model of the AFA18-02 sequence was constrained by a combination of short-lived
276 radionuclides, ^{14}C measurements and seasonal laminae visual and microscopic counting along the core
277 sequence . A continuous sampling step of 10 cm was applied over 173 cm of the AFA18-02 sequence
278 to determine ^{210}Pb , ^{226}Ra and ^{137}Cs activities. The ^{14}C measurements were performed on 9 organic matter
279 samples at the ARTEMIS facility, including 2 vegetal macro-remains and 2 fish bone samples using
280 ECHoMICHADAS, the Micro Carbon Dating System of the LSCE laboratory (Tab. 1).

281 **3.5 Rainfall-runoff modelling**

282 Observed streamflow time series at Tendaho Lake were extracted as daily timesteps from the GRDC
283 dataset (*station ID: 1577603, 11.683 N, 40.950 E, catchment area: 62 088 km², owner of original data:*
284 *Ethiopia - Ministry of Water Resources, Hydrology Department*). This time series is only available for
285 the 1990-2004 period, with numerous missing data during the 1994-1996 and the 2003-2004 periods.
286 To extend the temporal extension of the streamflow series, a rainfall-runoff model was used. The
287 monthly rainfall-runoff model GR2M (Mouelhi et al., 2006) was used using the airGR R package (Coron
288 et al., 2022, 2017). This conceptual and lumped model needs two continuous climatic time series as
289 inputs, precipitation (P) and potential evapotranspiration (E). GR2M has two parameters that need to be
290 calibrated for each studied catchment (cf. model diagram in Fig. S3). The NOAA 20CR (v3, Slivinski
291 et al., 2019) climatic reanalysis was extracted over the Awash River catchment at Tendaho Lake to
292 generate a monthly time series of precipitation and air temperature over the 1836-2015 period. A
293 monthly potential evapotranspiration time series was then estimated using the 20CR air temperature
294 time series and the Oudin et al. (2005) formula. The model parameters were automatically calibrated
295 using the Nash and Sutcliffe (1970) objective function over the 1990-2014 period, with an initialization
296 of the model reservoirs during the 1980-1989 period. Finally, the GR2M model parameters obtained for
297 the Awash River at Tendaho Lake were used over the 1836-2015 period to simulate streamflow over
298 this period.

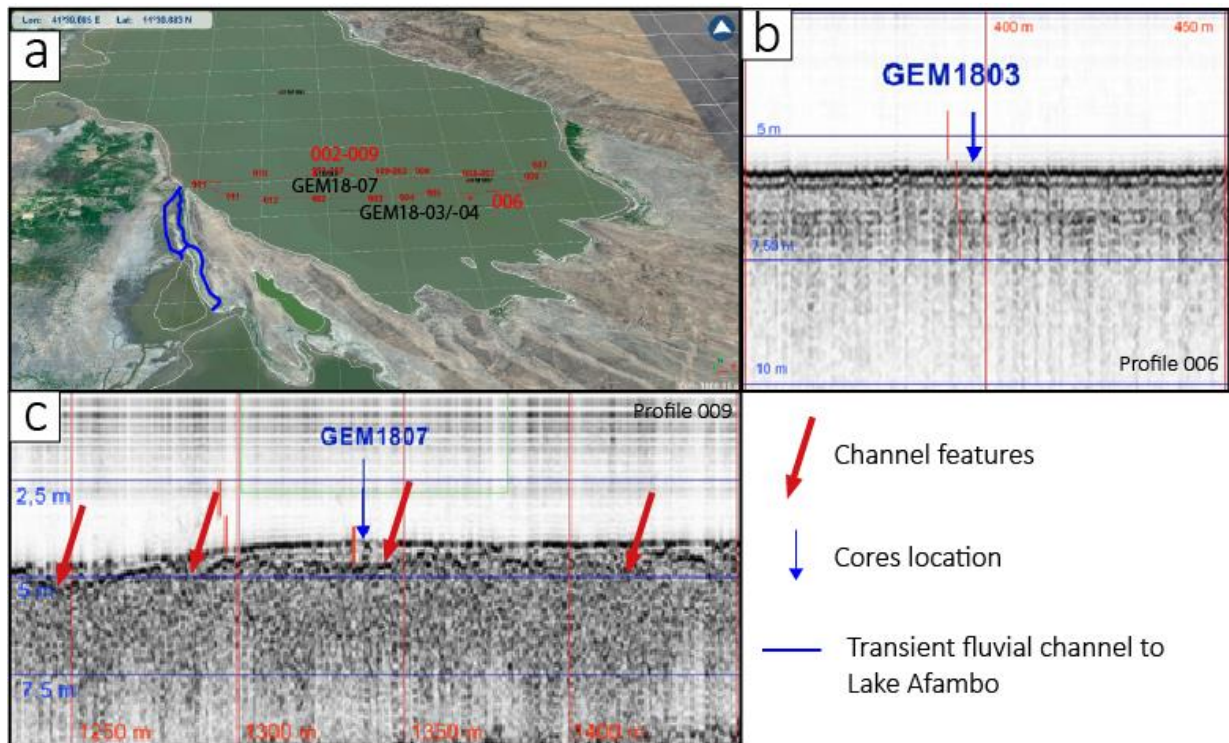
299 **4 Results**

300 **4.1 Seismic reflection imagery on Lake Gemeri**

301 Our chirp profiles provide a display of the bathymetry of Lake Gemeri for the first time. The average
302 measured water depth is 3 m with a maximum of 6 m in the southern part of the lake. Afambo Lake is
303 deeper, with a maximum depth of 18 m. The shallow depth (3 m on average) and very gentle slope of
304 Lake Gemeri are consistent with its location in the prodeltaic area of the Awash Plain.

305 Unfortunately, seismic penetration in Lake Gemeri is reduced to a few decimetres. Within the central
306 and eastern parts of the lake, an approximately 80 cm-thick upper sheet drape unit lies on a low-
307 amplitude reflector parallel to the lake bottom (profile 006, Fig. 2a, b). On the western part of the Gemeri
308 Lake, the upper sheet drape unit lies on a relatively strong amplitude reflector displaying a succession
309 of small highs and lows (few meters to tens of meters wide and a few decimetres deep) showing the
310 morphology of an erosional surface (profile 009, Fig. 2c). The succession of highs and lows along this
311 erosional surface correspond to small channels indicating periods of drying of the lake. Below these
312 reflectors, an extensive acoustic turbidity facies showing similarities with gassy facies (Bertin and
313 Chaumillon, 2005; Garcia-Gil et al., 2002) is observed. Five measurements of total organic carbon from
314 core GEM18-03 on 2 m of sediment indicate values of approximately 8.5% (Sup. Mat. S5), which
315 suggests that the gas could have come from the decomposition of organic matter (algae or upper
316 vegetation) in the lake. The presence of gas in the Lake Gemeri sediment is likely, given the high organic
317 productivity in this lake and the high content in organic matter in the sampled sediments and
318 sequestration of organic matter that often occurs in anoxic fine sediments (Bertin and Chaumillon, 2005;
319 Garcia-Gil et al., 2002; Roussel et al., 2009).

320



321
 322 **Figure 2:** Seismic reflection imagery on Lake Gemeri: **a)** 3D satellite image projection of southern Lake Gemeri (LANDSAT)
 323 with the location of the seismic profiles and of the cores reported in Figs. b and c; **b)** 006 seismic profile with the location of
 324 GEM18-03 core (blue arrow); **c)** 009 seismic profile with the location of GEM18-07 core (blue arrow) and of channel features
 325 (red arrows).

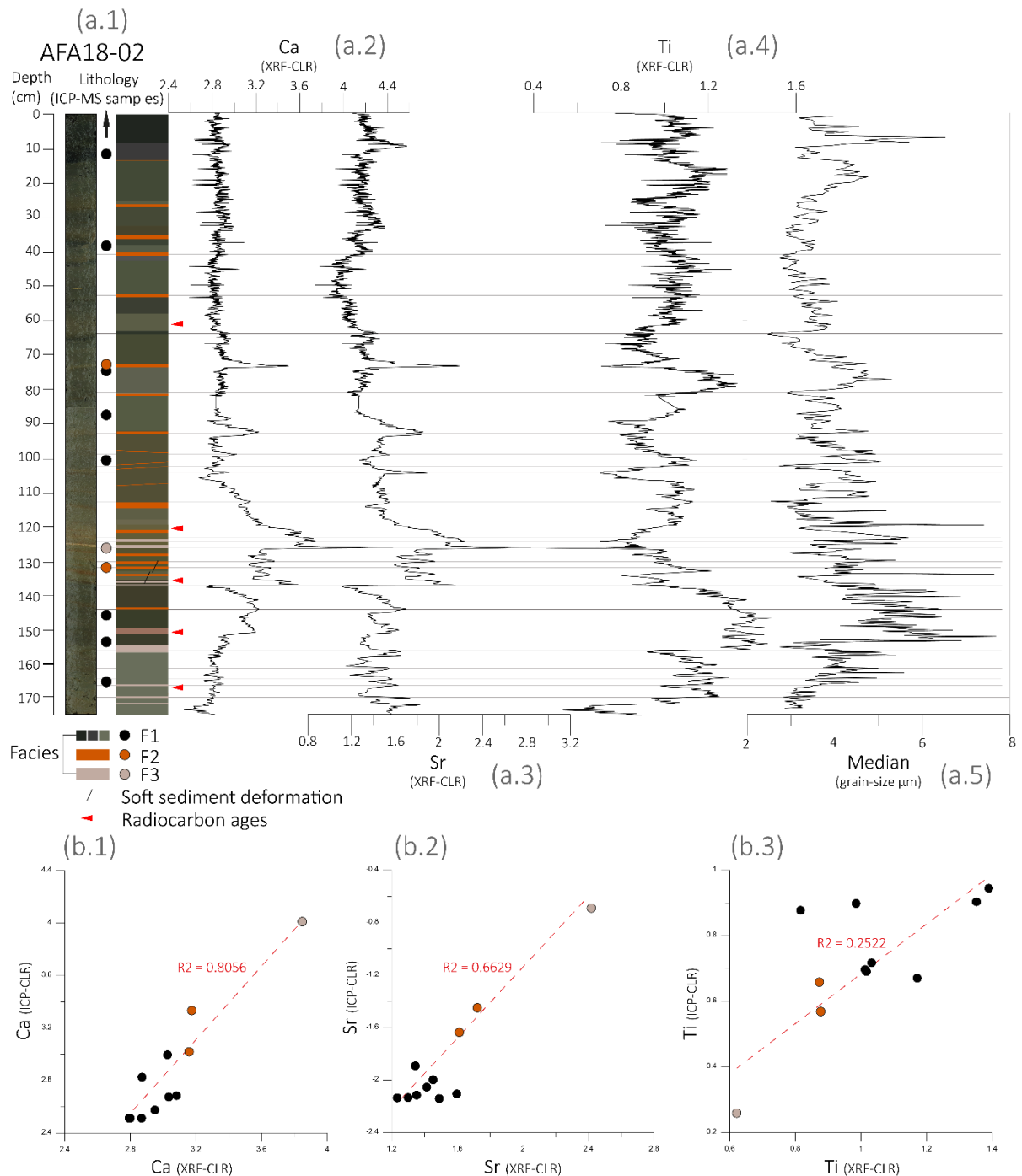
326 4.2 Sedimentology and geochemistry results

327 4.2.1 AFA18-02

328 The 173 cm-long sediment of AFA18-02 consists of undisturbed laminated sediments showing a clay-
 329 silty texture (Fig. 3a.1). A median size of 3 and 7 μm was measured at 2 mm resolution along the 173
 330 cm of the core, indicating that the lake's sedimentation did not record any extreme coarse or erosional
 331 event (Fig. 3a.5). Along the core, the first striking characteristic of this sequence is the succession of a
 332 couple of distinct facies systematically composed of brownish-grey coloured pluri-centimetric layers
 333 (Facies-1; F1) alternating with orange/brown coloured pluri-millimetric layers (Facies-2; F2) and
 334 sometimes associated with millimetric white beds (Facies-3; F3, Fig. 3a.1, 4b.1). Thirty-two couplets
 335 were hence identified, over the entire 173 cm sediment sequence.

336 The major element distribution measured for 11 discrete samples (Tab. 1) indicates SiO_2 values
 337 oscillating between 25 and 46%, TiO_2 values between 0.7 and 1.7% and a high concentration in iron of
 338 approximately 8%. Carbonate content values oscillate between 6 and 24% (Tab. 1). From the discrete
 339 samples, the coefficient of correlation between Ca and Sr is $R^2 = 0.97$. This suggests that the source of
 340 the carbonaceous component does not change along the 173 cm. Thanks to PCA analyses, 3 geochemical
 341 end members from Dim.1 (53,67%)/Dim.2 (23,43%) were differentiated (Fig. S4): The first one (EM1)
 342 yields major elements Al, Si, Fe, Ti, K, Zr and Mn with high positive loading on Dim1. The second end-
 343 member (EM2) gathers elements composing carbonates (Ca and Sr) and elements involved in the

344 evaporitic succession of minerals (S, Mg, Na) with high positive loading on Dim2 and positive loading
345 on Dim1. The third end-member (EM3) includes only Br negative loading on Dim1 and Dim2, which
346 is often used as a proxy for autochthonous organic matter in lakes (Bajard et al., 2016; Lefebvre et al.,
347 2021). The PCA factor map ascribes F1 layers into the EM1 area and the F2/F3 layers into the EM2
348 area (Fig. S5). Consequently, we selected Ti, Sr, and Ca to geochemically characterize the F1 and F2/F3
349 facies. A good plot correlation between CLR transform XRF and ICP–MS measured elemental values
350 (Fig. 3b) provides reliable Sr and Ca XRF data to geochemically characterize the three different
351 sedimentary facies along the core sequence. F1 is composed of microlaminated clays enriched in Ti, Si
352 and Fe elements (Fig. 3b.3). The F1 thickness varies substantially along the core, with an average
353 thickness of ~3 cm between 173 and 137 cm, a thickness of ~1 cm between 137 and 120 cm, a thickness
354 of 3.5 cm between 120 and 80 cm, and a thickness of ~9 cm between 80 and 0 cm. F2 (0.5-1 cm
355 thickness) is composed of microlaminated clay, diffused secondary carbonate impregnations (sparite)
356 and sporadic Fe-Mn nodules. Geochemically, the F2 layers are slightly enriched in Ca and Sr elements
357 (Fig. 3a, 3b). F3 (0.3-0.5 cm thickness) is composed of a massive-to-microlaminated micritic/sparitic
358 matrix strongly enriched in Ca and Sr elements (Fig. 3a, 3b, 7b.1). Soft sediment deformation has been
359 observed between 130 and 140 cm, evident in sub-vertical microfaults along the laminae, showing a
360 max deformation offset of ~3mm.



361
 362 **Figure 3:** Geochemical (XRF and ICP-MS) and sedimentological results on AFA18-02 core: **a.1)** Picture and lithology with
 363 the location of the sampling areas for ICP-MS analyses (dots); **a.2)** Ca XRF-(CLR) values; **a.3)** Sr XRF-(CLR) values; **a.4)**
 364 Ti XRF-(CLR) values; **a.5)** Grain size median; **b.1)** Correlation plot between Ca XRF-(CLR) and ICP-MS-(CLR) values; **b.2)**
 365 Correlation plot between Sr XRF-(CLR) and ICP-MS-(CLR) values; **b.3)** Correlation plot between Ti XRF-(CLR) and ICP-
 366 MS-(CLR) values.

367 Grain size distributions indicate three general dominant modes, one sorted clay mode at approximately
 368 1 to 2 μm, one well-sorted mode at approximately 19 μm, and the third is less dominant and lies in the
 369 sortable silt range at approximately 50 μm (Fig. 4b.3).

370 F1 layers present pronounced 1-2 μm and 50 μm modes, with the second represented mode at 19 μm.

371 F2 and F3 are well sorted at approximately 40 and 126 μm.

372

Dept (cm)	F	Na2O	MgO	Al2O3	K2O	CaO	TiO2	MnO	P2O5	SiO2	Fe2O3 (T)	Cr	Ni	Ba	Zr	Sr
		%	%	%	%	%	%	%	%	%	%	ppm	ppm	ppm	ppm	ppm
12	F1	1,97	4,62	13,13	1,85	6,30	1,50	0,10	0,28	45,80	9,57				271,65	423,40
39	F1	1,69	4,44	12,79	1,83	6,27	1,21	0,11	0,28	43,42	8,67	71,83	70,30	306,67	266,19	430,11
72	F2	1,32	4,35	10,60	1,43	14,16	1,06	0,11	0,26	36,48	7,30	59,87	56,34	371,84	221,51	847,12
73	F1	1,61	4,17	12,55	1,83	7,51	1,48	0,12	0,27	42,86	8,73	72,51	61,19	319,30	268,68	450,51
90	F1	1,39	4,08	11,78	1,92	8,37	1,14	0,10	0,26	42,62	8,26	72,86	62,70	287,74	254,22	480,19
100	F1	0,69	3,34	12,12	1,47	9,47	1,13	0,17	0,26	41,62	8,21	71,16	66,15	300,95	247,09	397,81
127	F3	0,96	5,28	6,67	1,01	23,79	0,67	0,14	0,19	25,11	4,57	39,57	40,49	399,08	136,28	1545,29
132	F2	1,34	4,93	10,58	1,53	10,39	1,24	0,11	0,25	37,96	7,42	67,73	62,20	351,79	227,72	706,21
148	F1	1,65	4,18	12,78	1,86	8,08	1,69	0,14	0,28	43,70	8,89	83,73	65,71	367,12	263,87	505,26
152	F1	1,58	4,47	12,64	1,89	6,93	1,55	0,12	0,26	43,45	8,82	82,59	63,67	329,38	266,35	454,91
168	F1	1,38	5,81	11,69	1,78	5,99	1,13	0,10	0,23	41,84	7,80	69,70	63,29	285,02	246,98	523,07

373 *Tab 1: Major and trace element concentrations of the AFA18-02 core; F = Facies.*374 **4.2.2 GEM18-03/04**

375 The sediment of GEM18-03/04 is homogeneously clayey ($Q_{50} = \sim 2.4 \mu\text{m}$) and dark brown in colour
376 (Fig. 5) all along its 220 cm. The first 15 cm are highly liquefied, presenting a clayey texture with slight
377 laminations. Between 19 and 40 cm, we note the presence of polyhedral clay structure and rootlets pores.
378 Between 38 and 222 cm, we observed a homogenous clay texture interbedded by seven layers of
379 lacustrine shells (*Melanoides tuberculata*), leading to a visible change in porosity at approximately 62
380 to 67 cm, 80 cm, 90 cm, 112-114 cm, 124 cm and 140 cm (Fig. S19).

381 The major element distribution (measured for 5 samples by ICP-MS, Table S1, S2) indicates SiO_2
382 values between 42 and 49% and TiO_2 values between 1.2 and 1.5%. The carbonate content values
383 oscillate between 5 and 10% (Table S1, S2). The plots Si versus Al and Al versus Ca indicate an
384 anticorrelation between terrigenous and carbonated materials; (Fig. S20), suggesting that the carbonate
385 particles mainly originated from the lake and not from the terrigenous fraction supplied by the Awash
386 flood. Similarly, the coefficient for Ca versus Ti is anticorrelated, consequently we will represent the
387 ratio of terrigenous/authigenic sediment components using the Ti/Ca ratio (Croudace and Rothwell,
388 2015).

389 The evolution of the $\text{Log}(\text{Ti}/\text{Ca})$ ratio defines 5 geochemical units (Fig. 5b.1): Unit 1 (0 to 19 cm) is
390 characterized by a gradual increase in $\text{Log}(\text{Ti}/\text{Ca})$ values. Unit 2 (40 to 19 cm) is characterized by a
391 gradual increase in siliciclastic elements; Unit 3 (115 to 40 cm) presents an abrupt decrease in
392 $\text{Log}(\text{Ti}/\text{Ca})$ at its base, followed by a progressive increase in Ti; Unit 4 (210 to 115 cm) is characterized
393 by a high lithogenic contribution; Unit 5 (222 to 210 cm) presents a high carbonate content. Between
394 38 and 222 cm, seven shell beds are characterized geochemically by an increase in Ca and Sr values
395 (Fig. S19).

396 4.3 Chronology

397 4.3.1 Age model of Lake Afambo sediments

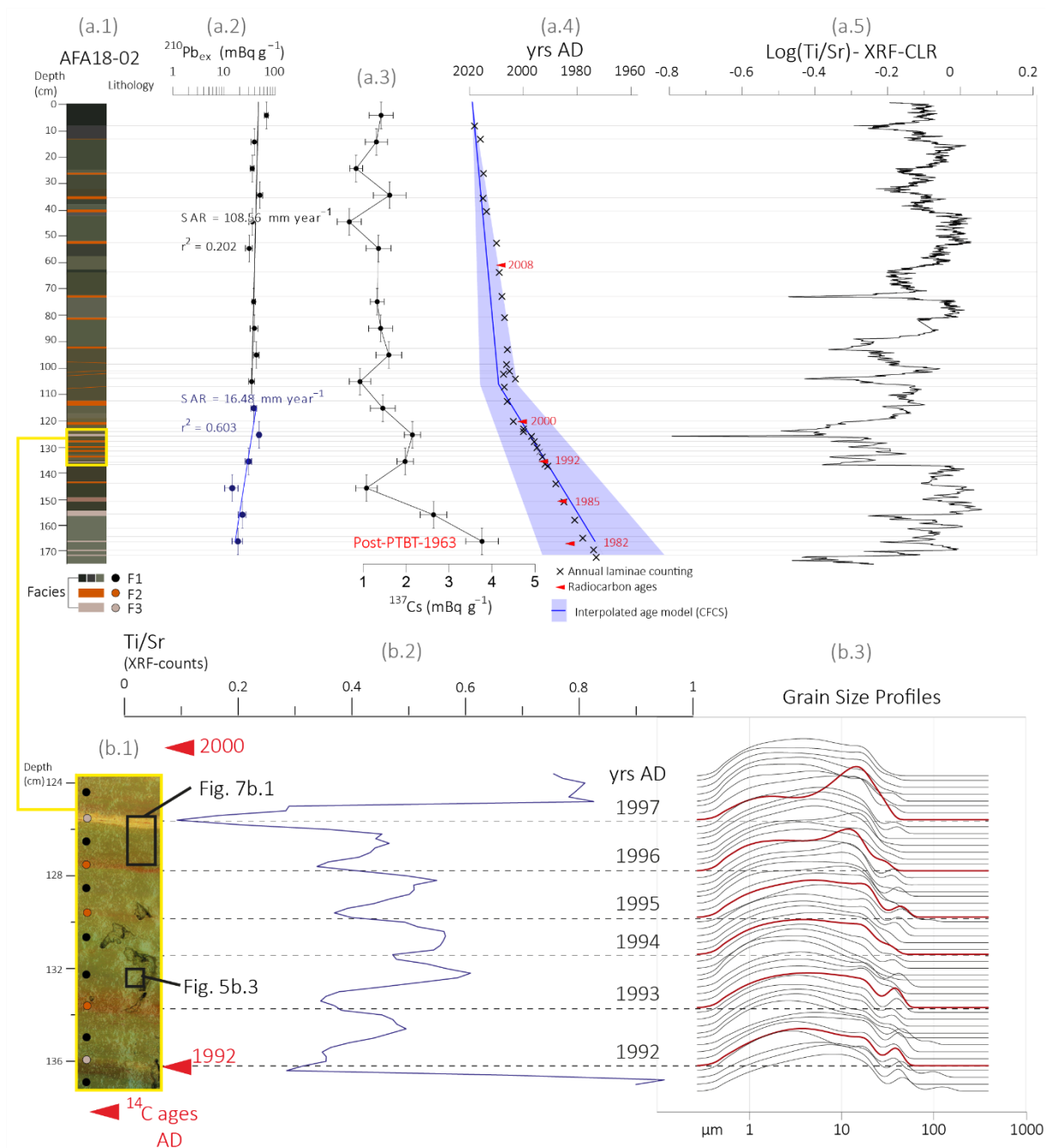
398 The 173 cm long AFA18-02 sediment was measured using gamma spectrometry to build an age model
 399 based on short-lived radionuclides (Fig. 4a.2, 4a.3). The ^{210}Pb excess profile first shows a slow decrease
 400 from the top to 105 cm and then a more rapid decrease between 105 and 170 cm until an activity of 26
 401 $\text{mBq}\cdot\text{g}^{-1}$. The use of a logarithmic scale to plot these data underscores a poorly constrained ($r^2=0.2$,
 402 related to very high sedimentation rate leading to low activity decreases) single-point alignment that
 403 shows a constant sedimentation rate of $108 \text{ mm}\cdot\text{yr}^{-1}$ for the first 105.8 cm and a better constrained
 404 ($r^2=0.6$) single-point alignment that shows a constant sedimentation rate of $16.5 \text{ mm}\cdot\text{yr}^{-1}$ between 106
 405 and 170 cm. The change in sedimentation rate occurred in 2009 ± 7 years. The ^{137}Cs profile shows an
 406 increase at the bottom of $4 \text{ mBq}\cdot\text{g}^{-1}$. This peak could be associated with the end of maximum nuclear
 407 weapon tests in 1963 CE (Foucher et al., 2021; Fig. 4a.3).

Depth (cm)	Lab ID	Material	Uncalibrated Age		Calibrated ages	
			BP \pm yrs (bulk)	F ¹⁴ C \pm (%)	2 σ cal CE (probability)	Median cal CE
10.5-11	SacA57084	Bulk sediment	315 \pm 30*			
44	SacA57085	Bulk sediment	640 \pm 30*			
61	GifA20055/ECHo3328	Fish Bone		1.0456 \pm 0.0029	[2008.88 - 2009.58] (30.3%)	2008
61	SacA59130	Bulk sediment	610 \pm 30*			
76	SacA57086	Bulk sediment	365 \pm 30*			
92	SacA57087	Bulk sediment	165 \pm 30*			
118-122	GifA20052/ECHo3259	Vegetal micro remains		1.0940 \pm 0.0179	[1993.78 - 2007.1] (90.3%)	2000
134.5-135	SacA57088	Bulk sediment	post 1950*			
134-136	GifA20053/ECHo3260	Vegetal micro remains		1.1364 \pm 0.0123	[1989.86 - 1996.94] (89.3%)	1992
149.5	GifA20056/ECHo3327	Fish Bone		1.2069 \pm 0.0031	[1984.82 - 1986.45] (52.8%)	1985
150	SacA59131	Bulk sediment	320 \pm 30*			

165.5-166.5	GifA20054/ECHo3261	Vegetal micro remains		1.2357 ± 0.0133	[1980.8 - 1982 1985.76A] (59.9%)	1982
165.5-166	SacA57089	Bulk sediment	post 1950*			

408 **Tab 2:** List of radiocarbon ages on bulk sediment (*), vegetal micro remains and fish bone material. Ages with * are
409 rejected. Calibration curve NH2 (Hua et al., 2013).

410 Among the 13 samples for ^{14}C ages (Tab. 2), the confrontation with the ^{210}Pb model shows that the
411 ^{14}C age measured on the bulk sediment organic matter was older, so these ages were systematically
412 rejected (* in Tab. 2). The older ages could be explained by the contamination of reworked micro-
413 organic matter particles from the Awash River catchment. The aging of radiocarbon dates on bulk
414 organic matter in large fluvial systems, such as the Awash River Basin, is often attributed to the
415 remobilization of fine organic particles from older deposits and soils eroded along the hydrographic
416 catchment. These particles are then deposited into terrigenous/detrital lacustrine sediments. In the case
417 of Afambo Lake sediments, the ages of bulk organic carbon exhibit an aging effect ranging between
418 approximately 100 and 600 years. Considering that the organic matter originates from flood deposits
419 during the monsoonal season (F1 facies), the hypothesis of remobilized fine particles is the most
420 probable explanation. A number of ^{14}C analysis were measured on fish bones and on vegetal micro
421 remains obtained from the micro sampling materials (Fig. S21 and S22). The five ages measured from
422 fish bone and vegetal micro remains are consistent with the ^{210}Pb -derived chronology and are considered
423 viable as part of the age model (Fig. 4a.4). 32 F1-F2/3 laminae couplets were identified and counted ,
424 which provides a 106 mm.yr^{-1} sedimentation rate that is highly comparable with the rate derived from
425 the CFCS model (108 mm.yr^{-1} ; Fig. 4a.2). Thus, the ^{210}Pb -derived age model confirms that a very high
426 sedimentation rate compatible with the F1 layers could correspond to one season of river-borne
427 discharge.



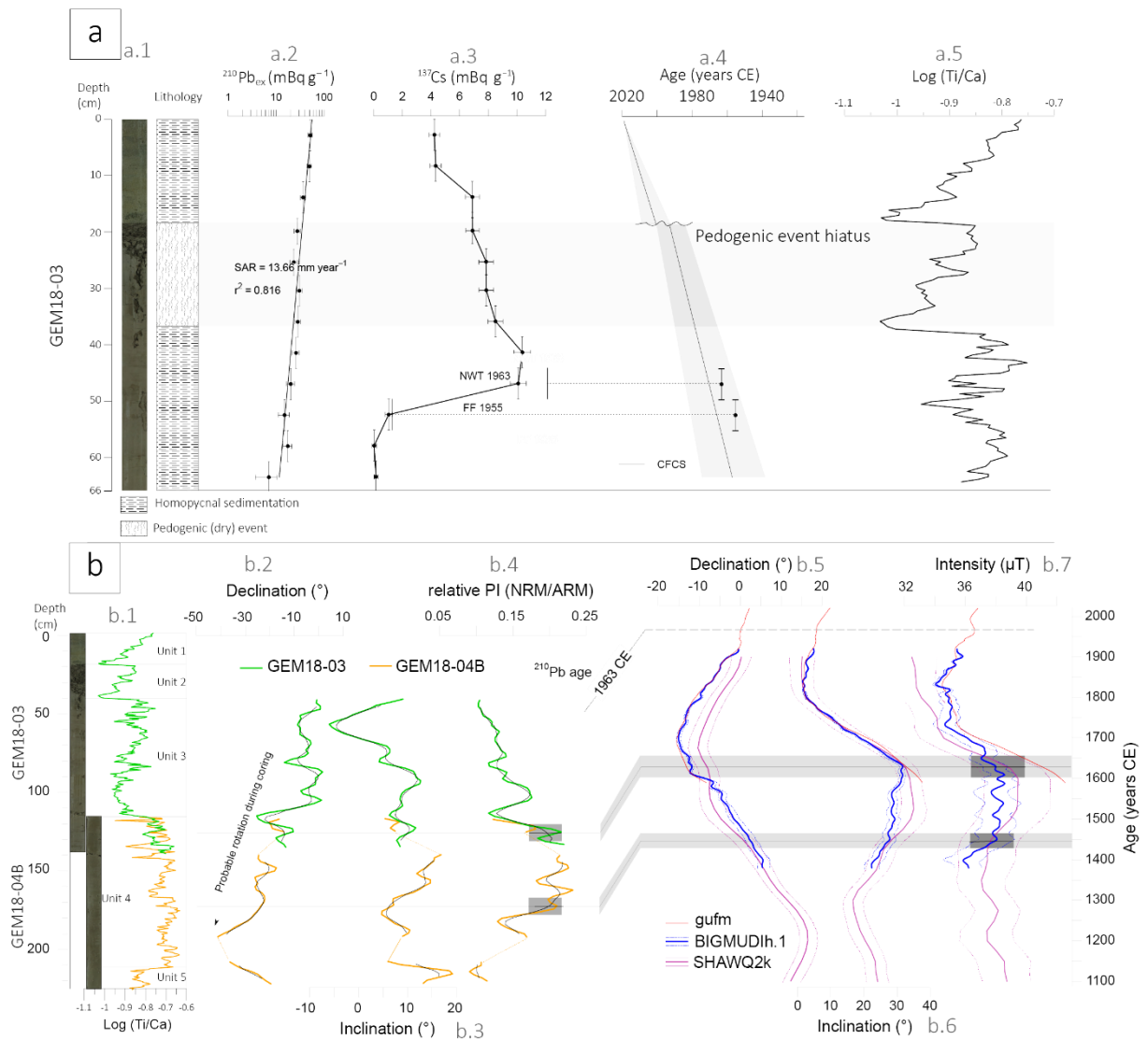
428

429 **Figure 4:** Age model of the AFA18-02 sequence: **a.1**) lithology; **a.2**) ^{210}Pb activity profile ($\text{mBq}\cdot\text{g}^{-1}$); **a.3**) ^{137}Cs activity profile
 430 ($\text{mBq}\cdot\text{g}^{-1}$); **a.4**) interpolated CFCS age model with annual laminae counting (crosses) and radiocarbon ages (red arrows); **a.5**)
 431 XRF $\text{Log}(\text{Ti}/\text{Sr})$ ratio transformed with a Centred Log Transformation package (Weltje and Tjallingii, 2008); **b.1**) focus on
 432 124-140 cm F1-F2/F3 couple counting; **b.2**) XRF Ti/Sr (124-140 cm) ratio curve with radiocarbon ages (red) and yrs
 433 CE/laminae counting; **b.3**) 124-140 cm grain size profiles (each 2 mm).

434 4.3.2 Age model of Lake Gemer

435 The upper 66 cm sedimentary sequence of the GEM18-03 core was measured using gamma
 436 spectrometry to build an age model based on short-lived radionuclides (Fig. 5a.1, 5a.2). The ^{210}Pb ex
 437 profile shows a gradual decrease from 51.8 to 7 $\text{mBq}\cdot\text{g}^{-1}$. The use of a logarithmic scale to plot these
 438 activities underscores a well-constrained ($r^2=0.8$) single-point alignment that shows a sedimentation rate
 439 of 13.66 $\text{mm}\cdot\text{yr}^{-1}$ for the first 66 cm (Fig. 5a.2). The ^{137}Cs profile reaches a clear peak between 42 and
 440 48 cm with a maximum activity $>10 \text{ mBq}\cdot\text{g}^{-1}$. This peak is attributed to the maximum nuclear weapon

441 tests in 1963 CE (Foucher et al., 2021) and is in accordance with the sedimentation rate derived from
 442 the $^{210}\text{Pb}_{\text{ex}}$ profile (Fig. 5a.2). Above this peak, ^{137}Cs activities slowly decrease, which suggests a large
 443 catchment area with input of ^{137}Cs already deposited in surface soil and transported by active annual
 444 floods (Fig. 5a.3). With the aim to provide a reliable chronology, sedimentary-pedogenic hiatus between
 445 1991 and 1997 has been removed from the age model (Figs. 5a.4, 6a.2).
 446 Among the 13 ^{14}C age samples (Sup. Mat. S9), the confrontation with the ^{210}Pb CFCS-derived
 447 chronology shows that the ^{14}C ages measured on organic matter are older by several thousands of years,
 448 and are therefore rejected with regard to the age model, such as is the case for 8 ages on bulk sediment
 449 for the Afambo core age model (Tab. 2). The five ages measured on lacustrine shells (*Melanoides*
 450 *tuberculata*; Murray, 1975) are still older than expected except for the age at 48.5 cm (Fig. S23).



451
 452 **Figure 5: a.1)** GEM18-03 upper section (first 66 cm) picture and lithology, **a.2)** $^{210}\text{Pb}_{\text{ex}}$ and **a.3)** ^{137}Cs profiles, NWT=Nuclear
 453 Weapons Tests; FF= FF 1955: first identification of ^{137}Cs in 1955; **a.4)** CFCS interpolated age model and **a.5)** Log(Ti/Ca)
 454 XRF count intensity. **b.1)** GEM18-03/04B composite section with Log(Ti/Ca) XRF count intensities; correlation between **b.2)**
 455 relative palaeo-intensity, **b.2)** inclination and **b.2)** declination measured on GEM18-03/04B with the **b.5 to b.7)** prediction at
 456 Lake Gegeri of three geomagnetic global models, BIGMUDIh.1 (in blue, Arneitz et al., 2021), gufm (in red, Jackson et al.,
 457 2000) and SHAWQ2k (in purple, Campuzano et al., 2019). BIGMUDIh.1 and SHAWQ2k.1 models are plotted with their 1- σ
 458 uncertainty envelope. The correlation is preferentially based on the BIGMUDIh.1 model (see text). For GEM18-03/04B, green
 459 and orange thick lines are raw results on GEM18-03 and GEM18-04B sections, respectively, while the thinner black curves

460 *show the variation after smoothing with 8-cm sliding windows. The two chronological tie-points are given by RPI, while the*
461 *secular variation of declination, and to a lesser extent of inclination is likely masked by disturbances during coring.*

462 To better constrain the age model and investigate the sedimentation rate below the first 66 cm dated by
463 short-lived radionuclides, we performed palaeomagnetic measurements with the objective of providing
464 chrono-markers in accordance with the palaeosecular variation in the geomagnetic field over the last
465 millennium (Fig. 5b; Crouzet et al., 2019). The rock magnetic and palaeomagnetic results are detailed
466 in Sup. Mat. S4. All rock magnetic results converge towards a homogeneous ferromagnetic mineralogy
467 below 40 cm, composed of almost pure magnetite of relatively fine grain size (pseudo single domain).
468 As the concentration in magnetic grains also does not vary significantly along the core, the magnetic
469 properties are very favourable to the determination of the relative palaeointensity (RPI; Fig. 5b.4). The
470 RPI results with the three possible normalizers (intensity of anhysteretic remnant magnetization ARM,
471 intensity of isothermal remnant magnetization IRM (low-field susceptibility)) are consistent, giving us
472 confidence in our RPI estimation even though it is based on only one core (Fig. 5b). The variations in
473 declination, inclination and RPI below 40 cm are plotted in Figs. 5b.2 and 5b.3. They are compared to
474 the prediction at Lake Gemeri of three geomagnetic global models: gufm (Jackson et al., 2000),
475 SHAWQ2k (Campuzano et al., 2019) and BIGMUD1h.1 (Arneitz et al., 2021; Figs. 5b.5 and 5b.6).
476 The correlation between the GEM18-03/04B results and the model is not straightforward. However,
477 ^{137}Cs and ^{210}Pb results from the top of the core allow us to propose a more solid chronological
478 framework of the sedimentary sequence. The almost continuous decrease in declination along the core
479 could suggest that the 190-222 cm depths could correspond to circa 1700 CE. However, the amplitude
480 of the decrease at approximately 40° is much larger than that in the models (approximately 15°), and we
481 strongly suspect that the declination record is biased by a slight progressive rotation feature during
482 coring. Short inclination oscillations in the core are not recognized in the model. Neither the inclination
483 minimum approximately 1840 CE nor the previous fast and regular decrease from 1630 CE are clearly
484 visible in GEM18-03/04B. Higher inclination values are in accordance with the model between 130 and
485 160 cm.

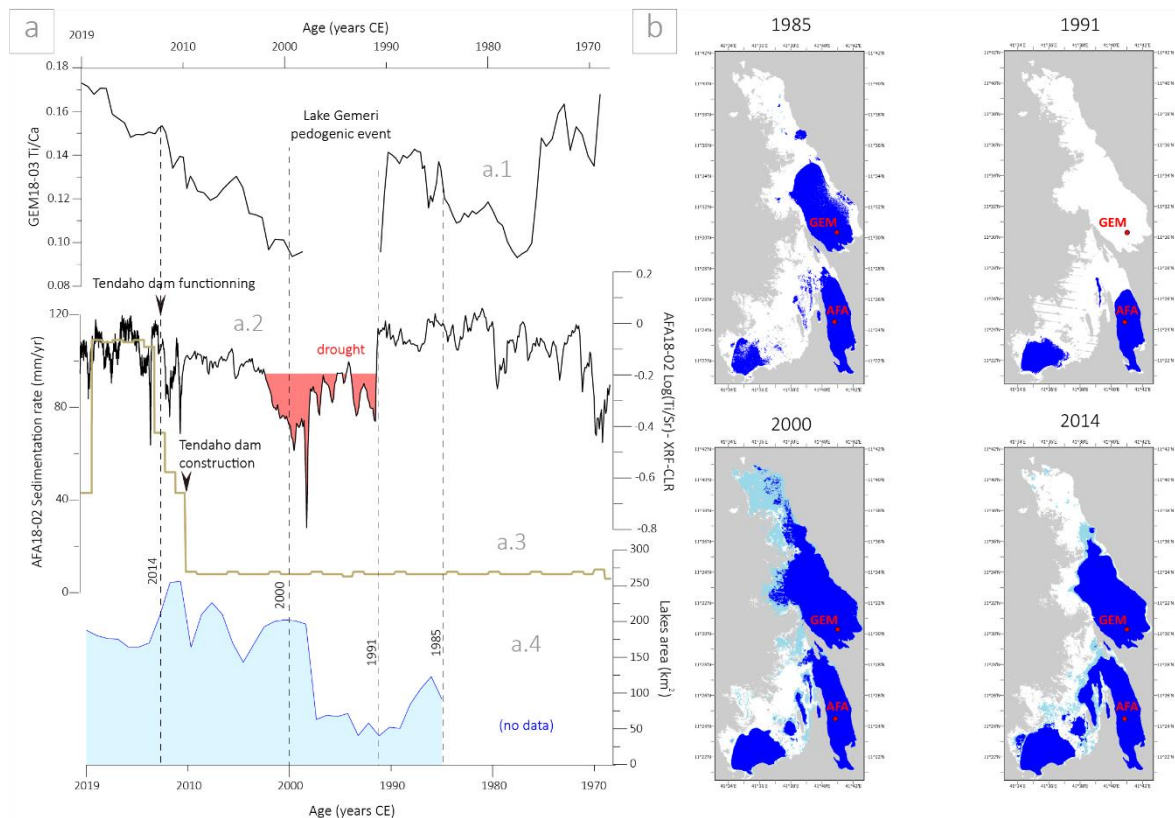
486 The period of higher intensity between the middle of the 15th c. and the first half of the 17th c. CE appears
487 to be recorded between 170 cm and 125 cm in GEM18-03/04B. This feature could provide two chrono-
488 markers to establish the age model, 120-130 cm corresponding to 1600-1650 CE and 167-177 cm to
489 1430-1460 CE. These two proposed tie points are rather consistent with inclination variations because
490 higher values of this parameter are observed in the two ranges of depth and age. The values of correlated
491 depths and ages should be considered approximate regarding the envelope error on the model and
492 because the predictions of global models are generally less reliable in intensity than in declination and
493 inclination (e.g., Brown et al., 2021). Palaeomagnetism measurements based on a single core cannot
494 provide a solid and high-resolution age model. However, the correlation with short-lived radionuclide
495 measurements on GEM18-03 and with the AFA18-02 age model allows us to propose some reliable
496 links with the Awash River hydro-sedimentary chronicles which are at decennial resolution. The

497 palaeomagnetic measurements provide confirmation that ^{14}C ages from GEM18-03/04B are too old, and
498 that these sediments do not exceed the last millennium.

499 **4.4 Changes in water surface area at Lakes Gemeri and Afambo, 1985 -** 500 **2019**

501 Since 1984, Landsat satellite image data have indicated that Lake Afambo experienced several
502 hydrological fluctuations without a complete drying of the lake. In contrast, Lake Gemeri partially dried
503 up starting in 1984, with a total drying up of the lake between 1990 and 1998 (Fig. 6, see Figs. S26 to
504 S28 for details). Then, between 1999 and 2000, the lake was completely refilled. Comparisons between
505 hydrological, geophysical, sedimentological and geochemical data will be discussed in the next
506 paragraphs Palaeolimnological and hydrological results from satellite image analyses might be not
507 perfectly linearly correlated due to sedimentary avulsions and earth surface processes along the river
508 course and between the two lakes (Phillips, 2003). Additionally, such offset can be attributed to the
509 combined $^{210}\text{Pb}/^{137}\text{Cs}$, counting couplets and radiocarbon age model errors which can span from 1yr to
510 7yrs.

511



512

513 **Figure 6:** Hydrosedimentary variability of Lakes Gemeri and Afambo during the last fifty years: **a.1)** Ti/Ca XRF ratio of
514 GEM18-03 sequence; **a.2)** Ti/Ca XRF ratio of AFA18-02 sequence; **a.3)** AFA18-02 sedimentation rate; **a.4)** lakes-level area
515 changes since 1985, Afambo + Gemeri; **b)** map representation of lake area changes in 1985, 1991, 2000 and 2014 CE; white
516 = no water, light blue = 1 month water (temporary water), blue = 12 months of water (permanent water), grey = no data.

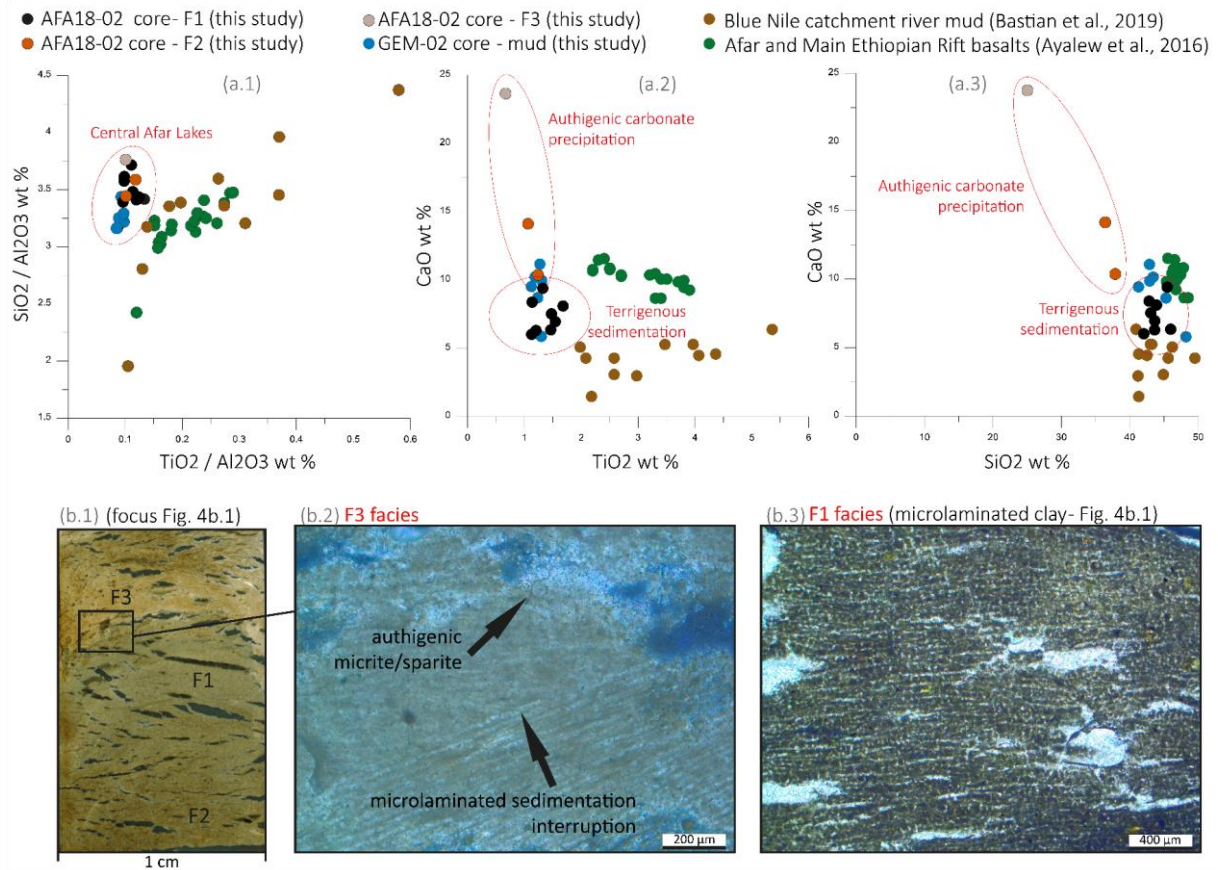
517 **5 - Discussion**

518 **5.1- AFA18-02 F1 and F2 significance**

519 **5.1.1 – F1 interpretation**

520 In the geological context of the Afar depression and Main Ethiopian Rift (MER), Si, Ti and Ca wt %
521 values of AFA18-02 and GEM18-03/-04B are compared with the same values of 11 mud samples from
522 the Blue Nile headwaters catchment (Bastian et al., 2019) and with 20 basalt samples from the Afar and
523 MER regions (Ayalew et al., 2016), corresponding to the sources of the Awash River catchment (Fig.
524 7). The Afar lake sediments are well-ranged in SiO₂ wt% values and partially included within the TiO₂
525 wt% values of the Ethiopian trap basalts and sediment sources, indicating that the origin of the
526 terrigenous inputs into the lakes is mainly represented by the solid discharge of the Awash River
527 catchment. The ~0.1% offset between the Afar lake sediments and the Ethiopian river sediments and
528 basalts can be attributable to a granulometric sorting effect. Similarly, the lithogenic signature
529 originating from the erosion of stratoid basalt series along the Awash River catchment is confirmed by
530 the ferromagnetic mineralogy of GEM18-03/-04B composed of almost pure magnetite (see section
531 §4.3.2 and Sup. Mat. S4).

532 Thick layers, high organic matter content, coarser grain size (D90 peaks of 25-30 μm) dominated
533 terrigenous elements (Si, Ti, Fe, Fig. 7a; EM-1 PCA, Sup. Mat. S4) characterize the F1 facies,
534 interpreted as a product of sedimentary load inputs from the Awash River during the wet season, which
535 is associated with the increase in monsoonal precipitation between March and August over the
536 catchment sources located on the Ethiopian Highland. The F1 patterns indicate that the solid load inflow
537 during the wet season corresponds to the formation of a particle suspended plume into the lake waters.
538 The lack of erosion features, the disconnection from deltaic geomorphic dynamics and the regular mode
539 of sedimentation (seasonal) indicate that Afambo is a basin characterized by yearly cyclic
540 hydrosedimentary functioning.



541

542 **Figure 7: Geochemical and microscopic analyses and interpretation of F1, F2 and F3 facies: a.1, 2, 3** SiO₂/TiO₂, CaO/TiO₂
 543 **and CaO/SiO₂ plots respectively, of Central Afar Lake sediments (black, orange and grey dots; This Study), Blue Nile**
 544 **catchment river muds (green dots; Bastian et al., 2019) and Afar and Main Ethiopian Rift Basalts (brown dots; Ayalew et al.,**
 545 **2016). b.1** Focus scan of this section 125-128 cm depth of AFA18-02 core (XPL); **b.2** Microphoto of F3 facies (XPL); **b.3**
 546 **Microphoto of F1 facies (PPL).**

547 5.1.2 – F2/F3 interpretation

548 The F2 and F3 facies appear to be enriched in CaO of ~10 wt% and ~24 wt%, respectively, and in Sr of
 549 ~800 ppm and ~1500 ppm, respectively, as a part of EM-2 of XRF PCA (Sup. Mat. S4). Difference
 550 between F2 and F3 is related to the CaO content: F2 is whitish-brown with a CaO ranged between ~10
 551 and ~15 wt%; F3 is white with a ~24 wt% CaO content. Microscopically, such enrichment is observable
 552 in the precipitation of sparitic and micritic minerals, showing an interruption of the microlaminated
 553 structure typical of F1 (Fig. 7b.2), and suggesting a sedimentation mode and carbonated mineral
 554 formation disconnected from the Awash River terrigenous inputs and suspension/sedimentation of fine
 555 particles in the lake. Moreover, F2 and F3 are clearly disconnected from the regional mineralogical
 556 source cortege (Fig. 7a.2 and 7a.3), indicating how such minerals originate from the lacustrine
 557 authigenic activity. Under high evaporation conditions during the dry season, sparitic minerals can be
 558 produced directly by chemical or biogenic precipitation into the lake.

559 Authigenic minerals precipitate when the evaporation rate exceeds the water inflow rate into the lake,
 560 leading to a switch from a terrigenous sedimentation pattern to the carbonate mineral precipitation mode.
 561 Considering high evaporation rates over the Lake Abhe basin (PE ~2000 mm/yr, Fig. 1e) which are
 562 concentrated during the dry season where there is low water inflow, authigenic precipitation of Ca and

563 Sr can represent the direct results of highly saturated waters and the related evaporative processes
564 (Cohen, 2003; Kylander et al., 2011; Martín-Puertas et al., 2011). Indeed, Ca and Sr are related to intra-
565 lake precipitation of CaCO_3 with Sr and Ca substitution. This substitution occurs when the chemical
566 concentration of lake waters reaches the point of carbonate saturation, as when lake waters are submitted
567 to a lowering of lake levels (Cohen, 2003). Accordingly, lake surface analyses show that enriched Ca
568 and Sr layers are concomitant with a lowering in Gemer and Afambo lake levels (Fig. 6a.2).
569 Consequently, F2 and F3 have been interpreted as the occurrence of the dry seasons along the Awash
570 River catchment over the last 50 years, and Ca and Sr elemental values can be used as a marker of
571 drought intensity.

572 **5.2 – Hydro-sedimentary mechanisms between Gemer and Afambo Lakes**

573 Despite their proximity, Gemer and Afambo Lakes present divergent patterns of sedimentation,
574 suggesting interdependent and complementary hydro-mechanisms. Located on the prodeltaic front,
575 Lake Gemer is the first and main receiver of the Awash River waters and sediment, which then overflow
576 into the Afambo basin (Fig. 1). Surprisingly, the ^{210}Pb activities of both lakes indicate a higher average
577 sedimentation rate in Lake Afambo ($\sim 10 \text{ cm.yr}^{-1}$) than in Lake Gemer ($\sim 1.36 \text{ cm.yr}^{-1}$).
578 Lake Gemer is characterized by a shallow water column (average of $\sim 3 \text{ m}$ depth measured during the
579 coring and seismic reflection imagery acquisition) in which the extension of the proximal seismic facies
580 into the central part of the basin is observed. Such evidence suggests how the inputs of the inflow waters
581 create sediment plumes that have expanded in three dimensions from the tributary mouth towards the
582 basin floor. Furthermore, the main homogeneous (non-laminated) structure of the deposits (Fig. 5)
583 suggests the input of continuous turbid currents (no variability in density) from the Awash River waters.
584 Such specific depositional patterns (deposit spatial geometry and sedimentary structure) are attributable
585 to homopycnal-like sedimentation, in which the density of the suspended sediment flow is equal to that
586 of the lake water (Bates, 1953; Chapron et al., 2007). In the absence of water stratification, homopycnal
587 conditions imply the homogeneous mixing of river and lake waters throughout the whole water column
588 by advection processes (Ashley, 2002; Bates, 1953; Chapron et al., 2007). In terms of depositional
589 processes, the occurrence of a homopycnal plume implies a short residence time of water and solid
590 suspended loads in lake waters, leading to reduced sedimentation on the basin floor (Campos et al.,
591 1989) and the development of contrasting sedimentation patterns between proximal and distal basins
592 (Chapron et al., 2007, 2006). Accordingly, most of the solid load transits through Lake Gemer,
593 producing a low sedimentation rate and erosive facies observed from seismic profiles, which have not
594 been recognized in the distal Lake Afambo basin (Fig. 2c). Furthermore, the shallow water patterns of
595 Lake Gemer ($\sim 3 \text{ m}$ average water-column depth) can promote the re-suspension of the bottom lake
596 sediments after the river floods or during wind-generated waves, reducing the sediment accumulation.
597 At 17 m water depth (coring site), Lake Afambo sediments show seasonal laminated structures (F1 and
598 F2/3). Facies alternation as well as the microlaminated structure documented in the F1 layers (Fig. 7b.3)

599 indicates the occurrence of rapid decantation processes shortly after each flood, thus suggesting slight
600 water column stratification and a difference between freshwater inputs and lake water density. Particle
601 sedimentation velocities calculated with the Stokes law confirm such observations, providing a mean of
602 ~3 days for the particles to sediment in Afambo lake (Tab. S3). Such sedimentary patterns combined
603 with the absence of erosive or turbiditic events suggest a hypopycnal character of the inflow waters/solid
604 load into Afambo Lake. Hypopycnal plume formation at the tributary mouth of Lake Afambo can be
605 made possible by the decrease in the current energy flow and by the loss of density of the waterfront by
606 the trapping of fine sediments into the deltaic marshes occurring between the two lakes (Fig. 1).
607 Accordingly, the <3.9 μm fraction is represented by 60-80% in Lake Gemeri and by 20-35% in Lake
608 Afambo (Figs. S24 and S25). Other factors that could influence the formation of hypopycnal plumes in
609 Afambo Lake are the reduced energy flow into the lake waters due to the endorheic patterns of the basin
610 (no outflow towards Lake Abhe) and a larger water-column depth.
611 The explanation of the general hydro-sedimentary modes of functioning of the two basins indicates **a**)
612 a first prodeltaic basin (Gemeri) with lower sedimentation rates, dominated clayey texture, erosive
613 processes and deltaic dynamics-dependant, which have recorded the general trends (centennial) of
614 hydrological fluctuations of the Awash catchment over a long period (~700 yrs) in our study; **b**) a second
615 distal basin (Afambo) with higher sedimentation rates, clayey texture and seasonal F1 and F2/3 deposits,
616 which records in high-resolution (interannual) the hydrological fluctuations of the Awash River
617 catchment during a short period (~50 yrs).

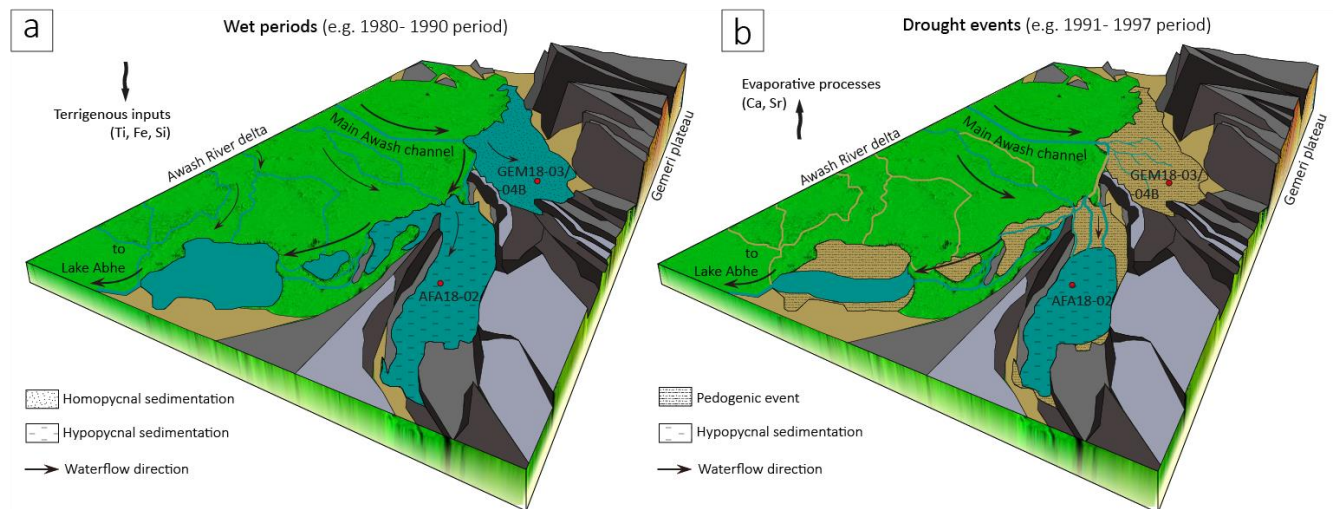
618

619 **5.3– Multi-centennial hydro-sedimentary trends from Lake Gemeri** 620 **sediments**

621 Similar to AFA18-02, PCA on XRF data of the Gemeri sequence (Fig. S6) show three main geochemical
622 end-members: the terrigenous one composed of Ti, Si, Al, K, Zr, Fe, Mn, and Mg; the evaporitic (Ca
623 and Sr); and the organic component (S and Br). Diachronic variations in these main components along
624 the GEM18-03/-04 core allow us to define two kind of periods: “Humid pluriannual periods” are
625 characterized by high terrigenous content such as Ti from high water flow activity of the Awash River.
626 Contrastingly, “dryer pluriannual periods” are characterized by the enrichment of Ca and Sr element
627 values interpreted as evaporative processes as a result of higher evaporation and reduced water inflow
628 into the lakes. Thanks to the composite short-lived radionuclides and palaeomagnetism age model on
629 the GEM18-03/04 sequence, we are able to discuss the general hydrological trends (centennial
630 resolution) for the period ranging between 1300 and 1964 CE.

631 Between 1300 and 1650 CE, relatively high and constant Ti/Ca ratio values were recorded (Fig. 5b.1).
632 This indicates how this period is characterized by high detrital inputs into the Lake Abhe basin, likely
633 induced by water inflow processes over the Awash River basin. Following a drop in Ti proxy between
634 1650 and 1750 CE, the catchment could have experienced a gradual increase in water and solid load

635 flow until 1964 CE, as deduced from the increase in Fe, Ti and Si elemental content. The last decade
 636 (1968-1964 CE) is thus characterized by higher solid load supplies compared to the following periods.
 637 Geomorphologically, during such decade, the Awash palaeo-delta was likely characterized by an
 638 anastomosing river network pattern that fed the prodeltaic lakes and marshes from the southwest to the
 639 northeast of the alluvial plain (Fig. 8a).
 640



641
 642
 643
 644

Figure 8: Schematic interpretative model of hydro-sedimentary patterns of the Awash River delta (including lakes Gemeri and Afambo) during enhanced wet periods (a) and drought events (b).

645 **5.4 - ~50-year-long seasonal drought and flood chronicle from Lake** 646 **Afambo**

647 In the AFA18-02 core, F1 and F2/F3 layers are interpreted as a result of the sedimentary interannual
 648 response of Central Afar Lake basins to wet and dry seasonal discharge of the Awash River. Thanks to
 649 the multi-proxy geochronological approach, we are able to propose a solid age model covering the
 650 period between 1969 CE and 2019 CE.

651 The aim of this section is to provide a wet and dry season magnitude chronicle for the last ~50 years
 652 across the Awash River basin through a) the estimation of the wet season inflow intensity recognized in
 653 F1 layers and b) the estimation of drought/evaporitic process intensities recognized in dry season F2/F3
 654 layers (see section §5.1 for the facies interpretation).

655 With the aim of reconstructing the intensity of the Awash River wet season intensities, we selected two
 656 proxies: the grain size and the thickness of the F1 layers. Thanks to well-established published data, we
 657 are able to propose an interpretation of the river energy discharge based on the grain-size data (e.g.,
 658 Campbell, 1998; Lapointe et al., 2012; Parris et al., 2010; Sabatier et al., 2022, 2017; Wilhelm et al.,
 659 2015). Indeed, the coarse grain size fraction (D90) has been successfully used to track hydrologic
 660 conditions, particularly the transport capacity and the stream velocity during flood events, such as the
 661 intensity of past floods (Gilli et al., 2013; Molinaroli et al., 2009; Parris et al., 2010). Similarly, previous

662 studies interpret the thickness of flood deposits in lakes as the total volume of solid material transported
663 and deposited during flood events (Jenny et al., 2014; Schiefer et al., 2011; Wilhelm et al., 2015, 2012).
664 Chronologically corresponding to the duration of the monsoonal rainy season and in absence of
665 turbiditic layers or singular events deposition sedimentary patterns (e.g. flash floods), the F1 layers are
666 not considered as a result of a unique flood event but as the sum of flood events that occurred during the
667 wet season. Consequently, we can consider the F1 layer thickness and D90 as proxies of the Awash
668 discharge intensity in terms of flow energy and the volume of solid load that occurred during the wet
669 monsoonal period between March and August. In our case, the striking similitudes between D90 peaks
670 and thickness of F1 layers (Fig. 9b, c) confirms the combination of proxies for tracking the flood season
671 intensities.

672 To reconstruct the intensity of the dry season, we use Sr and Ca elements and the Ti/Sr elemental ratio
673 (Fig. 9) as a marker of evaporative processes resulting from reduced water flow inputs and the
674 contraction of the lake surface as explained in detail in section §5.1.2. The relationship between
675 enhanced carbonate precipitation and drought intensity in Lake Afambo is evident in the F3 layer at 126
676 cm, corresponding to the 1997 CE dry season, in which the highest Ca and Sr values recorded in the
677 core correspond to the lowest lake level ever observed and the strongest impact of El Niño that has ever
678 been historically recorded over East Africa (Fig. 9; Palmer et al., 2023).

679 The comparison between Ti/Sr, F1 thickness and D90 proxies (Fig. 9a, b and c) shows a strong
680 relationship between physicochemical authigenic processes (carbonate precipitation and Sr enrichment
681 linked to evaporative trends in the dry season) and the Awash River solid load inputs into the lake (linked
682 to the increase or the reduction of water flow at the yearly scale). Consequently, we are able to discuss
683 the variability of the wet seasons and drought intensities in the Central Afar region over the last ~50
684 years.

685 Between 1969 and 1979, a gradual increase in both F1 thickness and D90 indicates a decennial
686 intensification of wet season solid/liquid Awash river discharge, with two years of demarcated wet
687 season floods in 1976 and 1978. Decrease of Ti/Sr indicate an enhanced dry season in 1969, 1978 and
688 1979. Between 1980 and 1990, a general and constant trend of high river discharge was recorded with
689 enhanced floods in the 1981, 1982, 1988 and 1989 wet seasons. A pronounced drought was recorded in
690 1983/1984.

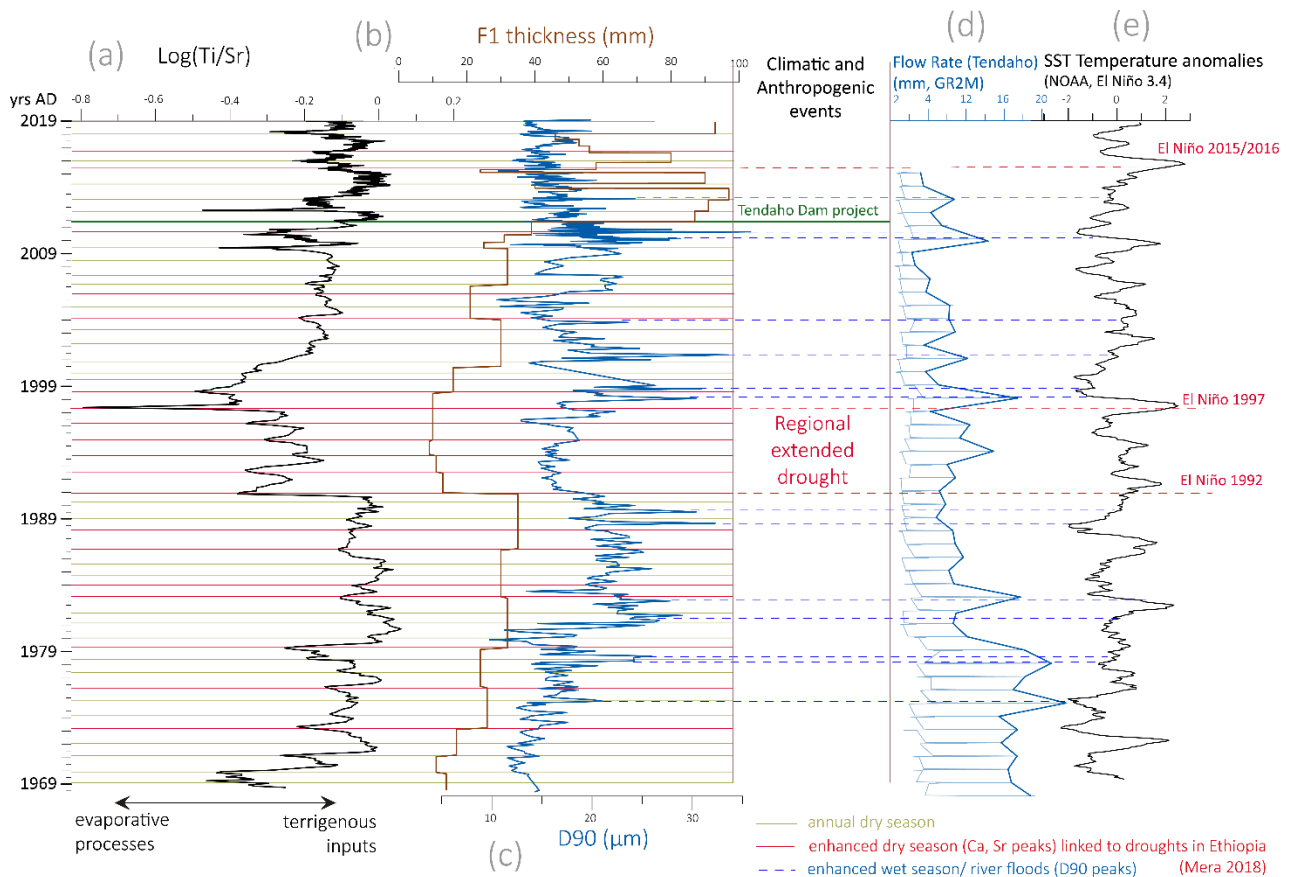
691 From 1991 to 1997, the occurrence of an abrupt lowering thickness of F1 and low and constant D90
692 indicate reduced river load inputs compared to the previous and following periods, suggesting a reduced
693 river discharge intensity during the wet season. Such weak river discharge is in accordance with the
694 lowest level recorded for Lake Afambo, the drying of Gemeri Lake (Fig. 6a.4) and high evaporative
695 processes of lake waters (Sr peaks), especially between 1991 and 1997, highlighting the occurrence of
696 the most severe drought period that has been recorded over the last ~50 years in the Central Afar Region.
697 During this period, Lake Gemeri dried up, evident in satellite image analyses and in the GEM18-03/-

698 04B lithology characterized by the development of a concomitant pedogenic horizon. During this time
699 the lake Gemeri was occupied by vegetation and incipient soil formation.

700 Between 1998 and 2010, constant Ti/Sr and increase of F1 thickness proxies indicate a gradual increase
701 in river terrigenous inputs in relation to weak dry season drought intensities, except for two years of dry
702 season droughts recorded in 2009 and 2010. The high variable D90 suggests the alternation between
703 yearly high- and low-energy inflow, highlighting a year-by-year hydrological instability of the Awash
704 River catchment for this period.

705 Since the 2010 wet season, the AFA18-02 sequence records a disproportionate increase in sedimentation
706 rate (Fig. 6a.3) and in yearly solid load volume inputs (F1 thickness Fig. 9b), in concomitance with a
707 reduced river energy discharge (low and constant D90) and an average lake water surface decrease of
708 $\sim 100 \text{ km}^2$ compared to the previous decade. Such a hydro-sedimentary anomaly could be attributable to
709 a strong anthropogenic impact such as that induced by the construction of the Tendaho Dam and the
710 related Tendaho reservoir (Dereje et al., 2018; Yemane, 2008). Indeed, between 2010 and 2014, the dam
711 project included the reorganization of the hydrographic network of the Lower Awash plain with the
712 massive development of irrigation channels, sugarcane cultivation and a sugar factory (corresponding
713 to the alluvial plain area in Fig. 1b). The increase in solid load discharge could thus be linked to the
714 disproportionate intensification of local soil erosion induced by artificial channel digging and
715 agricultural exploitation of the lower Awash plain. Accordingly, the reduced river flow energy and lake
716 surfaces are related to the water retention of the artificial Tendaho reservoir at the mouth of the Lower
717 Awash plain. For this period, our geochemical and sedimentological data are not discussed in terms of
718 regional climate-induced drought and flood intensities because they are partially disconnected from the
719 regional hydrological dynamics of the Awash River catchment.

720



721

722 **Figure 9:** Fifty years of Awash seasonal flood/drought magnitudes and their connection with ENSO events recorded in the
 723 AFA18-02 sequence: **a)** Log(Ti/Sr) XRF ratio; **b)** F1 thickness; **c)** D90; **d)** water flow rate at Tendaho (mm, GR2M); **e)** SST
 724 temperature anomalies (NOAA, El Niño 3.4) with indicated annual F2 laminae (dry season, yellow lines), enhanced dry
 725 interannual events (red lines) and enhanced wet season/river flood periods (blue lines).

726 **5.5 Awash River wet/drought seasonality and their comparison with** 727 **ENSO impacts in Horn of Africa**

728 The comparison between our wet/dry season intensity reconstruction, the flow rate modelling of the
 729 Awash River at Tendaho Lake, and the SST anomalies of the NOAA El Niño model allow us to discuss
 730 the high-resolution seasonal hydro-climate variability of the Awash River catchment in relation to El
 731 Niño atmospheric anomalies (Fig. 9).

732 We have observed a generally stronger drought in our record during El Niño years, which are known to
 733 be associated with low discharge, while La Niña years correspond with relatively high discharge (Abteu
 734 et al., 2009; Amarasekera et al., 1997; Camberlin et al., 2001; De Putter et al., 1998; Eltahir, 1996; Wang
 735 and Eltahir, 1999; Zaroug et al., 2014; Fig. 9). We have also observed that the occurrence of extreme
 736 wet season conditions at the onset of La Niña periods seems proportional to the gradient amplitude
 737 between positive and negative ENSO SST temperature anomalies, as is evident in 1998 (Fig. 9).
 738 Accordingly, the D90 variability of the AFA18-02 core indicates the occurrence of high hydrological
 739 activity during 1975, 1978, 1981/82, 1988/89 years following El Niño-induced droughts documented in
 740 1975/76, 1978/79, 1982 and 1987/88 in Ethiopia (Mera, 2018). Overall, along the Afambo sequence, all

741 major El Niño-induced droughts are systematically well recorded by our proxy of drought intensity (red
742 lines Fig. 9; Mera, 2018).

743 High evaporation processes and low fluvial solid load inputs recorded in the AFA18-02 sequence
744 suggest that along the Lower Awash valley, the period between 1991 and 1997 experienced the most
745 extreme and continuous drought in the region of the last ~50 years (Fig. 9). In the Lake Abhe basin,
746 such an event caused the complete drying of Lake Gemeri and a substantial lowering of Lake Afambo
747 (Fig. 6b), suggesting loss of water capacity of the lower Awash plain agricultural fields. In East Africa,
748 the 1997/1998 El Niño tended to have significant socio-economic and health impacts on populations
749 even if it was not as extreme or as widespread as that of 1984 (Palmer et al., 2023). In contrast, the
750 sedimentary record of the Afar lakes has revealed that the 1997 drought was more intense than the 1984
751 drought. Such discrepancy can be attributable to strong regional variability, with particularly arid areas
752 such as the Afar region being more impacted by drought than other East African regions. Accordingly,
753 *United Nations Emergencies Unit for Ethiopia* reports highlight how the 1997 drought was particularly
754 virulent in the Somali Regional state and the Afar, located in the southeast of the Horn of Africa (Borton,
755 1997). As a result of low rains in 1996 and 1997, more than 275,000 people in the Afar Regional State
756 were reported to be affected by drought.

757 At the scale of the Horn of Africa, 1997 is considered to have had socioeconomic impacts principally
758 related to the La Niña flooding events. From October to December 1997, exceptionally heavy rains
759 seriously affected food production throughout Eastern Africa (CARE, 1998; Nicholson, 2017).
760 Accordingly, immediately after the extreme extended drought between 1991 and 1997, we observe a
761 disproportionate increase in Awash River solid load inputs that were concomitant with La Niña (Fig. 9).
762 From April 2016 to December 2017, the southeastern regions of the Horn of Africa experienced the
763 strongest drought of the last ~40 years which have been linked to the El Niño 2015 event (MacLeod and
764 Caminade, 2019; Mera, 2018). Even if modulated by the Tendaho dam, we observe three consecutive
765 years of reduced sedimentation rates and unwanted evaporation processes from the Afambo sequence
766 indicating that the lower Awash valley had been impacted by anomalously weak rainy seasons in 2015
767 and 2016. In the nearby Somali region, such events triggered acute food shortages and malnutrition
768 exacerbated by a shortage of potable water that led to disease outbreaks, which affected more than six
769 million people (FSNAU, 2022; WBG, 2018).

770 The AFA18-02 sequence has been shown to be an exceptional record of anomalous hydrological events
771 in the region, but quantitative data for regional to local climate change impacts are still lacking. Indeed,
772 our record provides high-resolution wet season and drought magnitude records, highlighting some
773 similarities and divergences compared to historical and instrumental records, which are necessary for
774 the improvement of Eastern African climate prediction models. Such discrepancy can be attributed to
775 the lack of comprehensive instrumental data for the lower Awash River catchment area. Specifically,
776 the flow rates in Tendaho have been modeled using discontinuous and low-resolution datasets. The
777 simulated streamflows at Tendaho are subject to uncertainties arising from several factors: the rainfall-

778 runoff model itself, the calibration of its parameters based on limited observed streamflow data
779 (available only for the period 1990-2014), and the uncertainties in the meteorological inputs (sourced
780 from the NOAA 20CR global reanalysis). This data merits integration into models to test different
781 external forcings and large-scale climate teleconnections and feedbacks (vegetation, dust concentration,
782 Indian Ocean Dipole, South Atlantic SST, relationship between ENSO and summer monsoon
783 variability), which have affected inter-annual to multi-centennial hydrological variability in East Africa.

784 **6 Conclusion**

785 In this study, we have demonstrated that the hydro-sedimentary patterns of Central Afar Lakes
786 (Ethiopia) are highly sensitive to changes in yearly precipitation over the Awash River catchment. Using
787 a solid age model, sedimentological and geochemical proxies and microscopic observation on two
788 lacustrine cores cross-referenced with a lake surface reconstruction model from satellite images and
789 seismic imagery, we provide a high-resolution seasonal record of Awash River wet seasons/droughts
790 covering the last ~50 years. Atmospheric anomalies linked to ENSO SST variability are the main factors
791 determining hydrological instability over the Central Afar basin during the last fifty years in terms of
792 flood hazards and drought periods. Between 1969 and 1989, our record shows increased wet season
793 flood activity of the Awash River linked to La Niña, with a moderate impact of the 1984 El Niño on
794 evaporative conditions in the Lake Abhe basin. Between 1991 and 1997, we highlight the occurrence of
795 the strongest prolonged drought ever recorded in the Central Afar Lake region, and demonstrate
796 similarities and divergences between our data and instrumental and historical drought records. This
797 study provides new unpublished data on the impact of ENSO in the region and confirms the utility of
798 this unique quantitative record for the improvement of future regional climate predictions. From a local
799 perspective, we provide robust evidence to demonstrate how the construction of the Tendaho dam along
800 the Awash River associated with extensive agricultural management, strongly affected the
801 hydrosedimentary balance of the Lower Awash Valley from 2010, likely resulting in a disproportionate
802 increase in local soil erodibility along the alluvial plain.

803 The reactivity of local to regional hydrology and soil to global changes remains understated in East
804 African climatic models. This paper demonstrates the importance of studies on regional hydro-system
805 feedbacks to global atmospheric anomalies, to better understand and mitigate the sometimes catastrophic
806 effects of global warming in extreme environments such as the Afar, especially in the context of current
807 climate-induced food insecurity in East Africa (2022-2023 season) and dire predictions for what is
808 ahead.

809

810 **Code and Data availability**

811 The detailed core location and coring information are available on the Cyber Carothèque Nationale of
812 CNRS (<https://cybercarotheque.fr/>). All analytical data presented in this manuscript are available in the
813 Supplementary Material document.

814
815

816 **Author contribution**

817 **C. Mogni:** Conceptualization, Data curation, Formal analysis, Investigation, Supervision, Validation,
818 Visualization, Writing – original draft preparation - review and editing.

819 **M. Revel:** Conceptualization, Funding acquisition, Investigation, Project administration,
820 Supervision, Writing – original draft preparation– review & editing.

821 **E. Chaumillon:** Conceptualization, Investigation, Formal analysis, Data curation, Visualization,
822 Writing– original draft preparation – review & editing.

823 **E. Malet:** Formal analysis, Investigation, Methodology, Resources.

824 **T. Coulombier:** Formal analysis, Investigation, Methodology, Resources.

825 **P. Sabatier:** Conceptualization, Data curation, Formal analysis, Investigation, Resources,
826 Visualization, Writing– original draft preparation – review & editing.

827 **P. Brigode:** Conceptualization, Data curation, Formal analysis, Investigation, Writing– original draft
828 preparation – review & editing.

829 **G. Hervé:** Conceptualization, Data curation, Formal analysis, Investigation, Visualization, Writing –
830 original draft preparation – review & editing.

831 **A.-L. Develle:** Data curation, Formal analysis, Investigation, Methodology, Resources.

832 **L. Schenini:** Data curation, Formal analysis, Investigation.

833 **M. Messous:** Data curation, Formal analysis, Investigation, Methodology, Resources.

834 **G. Davtian:** Data curation, Formal analysis, Investigation, Methodology, Resources.

835 **A. Carré:** Formal analysis, Investigation, Methodology, Resources.

836 **D. Bosch:** Formal analysis, Methodology, Resources.

837 **N. Volto:** Conceptualization, Data curation, Formal analysis, Investigation, Writing – original draft
838 preparation – review & editing.

839 **C. Méndard:** Project administration, Resources.

840 **L. Khalidi:** Conceptualization, Funding acquisition, Project administration, Supervision, Writing -
841 review & editing.

842 **F. Arnaud:** Conceptualization, Investigation, Project administration, Data curation, Supervision,
843 Ressources, Writing – original draft preparation– review

844

845 **Competing Interests**

846 The authors declare that they have no conflict of interest

847

848 **Acknowledgements**

849 The CLIMAFAR (PIs: L. Khalidi & M. Revel) December 2018 coring operations were carried
850 out in the framework of the VAPOR-Afar project (PI: L. Khalidi) with a permit granted by the
851 Ethiopian Authority for Research and Conservation of Cultural Heritage (ARCCH, Addis
852 Ababa, Ethiopia) in collaboration with the Afar Bureau of Tourism & Culture. Funding for
853 CLIMAFAR was granted by the French government, and managed by the Agence Nationale de
854 la Recherche under the Investissements d'Avenir UCAJEDI project, reference no. ANR-15-
855 IDEX-01 . XRF-Core Scanner and thin section fabrication were performed at the EDYTEM
856 laboratory with funding from the CLIMAFAR grant. XRD analyses were funded by a
857 University Cote d'Azur doctoral grant (C. Mologni). Radiocarbon dating was performed with
858 funding from an ARTEMIS grant and support from the Geoazur laboratory (M. Revel) using
859 the MIChadass facilities (Christine Hatté; LSCE – UMR 8212 CEA-CNRS-UVSQ). The authors
860 thank the Laboratoire Souterrain de Modane (LSM) facilities for the gamma spectrometry
861 measurements and Environnement, Dynamique et Territoires de Montagne (EDyTeM) for the
862 X-ray fluorescence analyses (A.-L. Develle). We would like to thank the Ethiopian ARCCH,
863 the Afar Bureau of Tourism & Culture and the French Center for Ethiopian Studies (CFEE) for
864 their authorization and support with regards to fieldwork and logistics. We also thank Dr.
865 Tatiana Theodoropoulou and Dr. Lucie Coudert for the fish species determination of the
866 AFA18-02 core sequence.

867

868 **References**

- 869 Abtew, W., Melesse, A.M., Dessalegne, T., 2009. El Niño Southern Oscillation link to the Blue
870 Nile River Basin hydrology. *Hydrological Processes* 23, 3653–3660.
871 <https://doi.org/10.1002/hyp.7367>
- 872 Amarasekera, K.N., Lee, R.F., Williams, E.R., Eltahir, E.A.B., 1997. ENSO and the natural
873 variability in the flow of tropical rivers. *Journal of Hydrology* 200, 24–39.
874 [https://doi.org/10.1016/S0022-1694\(96\)03340-9](https://doi.org/10.1016/S0022-1694(96)03340-9)
- 875 Arnaud, F., Poulénard, J., Giguët-Covex, C., Wilhelm, B., Révillon, S., Jenny, J.-P., Revel, M.,
876 Enters, D., Bajard, M., Fouinat, L., Doyen, E., Simonneau, A., Pignol, C., Chapron, E.,
877 Vannièrè, B., Sabatier, P., 2016. Erosion under climate and human pressures: An
878 alpine lake sediment perspective. *Quaternary Science Reviews* 152, 1–18.
879 <https://doi.org/10.1016/j.quascirev.2016.09.018>
- 880 Arnaud, F., Sabatier, P., 2022. Lakes as Recorders of Earth Surface Dynamics From Yearly to
881 Plurimillennial Time-Scales, in: Mehner, T., Tockner, K. (Eds.), *Encyclopedia of Inland
882 Waters (Second Edition)*. Elsevier, Oxford, pp. 439–452.
883 <https://doi.org/10.1016/B978-0-12-819166-8.00125-0>

884 Arneitz, P., Leonhardt, R., Egli, R., Fabian, K., 2021. Dipole and Nondipole Evolution of the
885 Historical Geomagnetic Field From Instrumental, Archeomagnetic, and Volcanic Data.
886 Journal of Geophysical Research: Solid Earth 126, e2021JB022565.
887 <https://doi.org/10.1029/2021JB022565>

888 Ashley, G.M., 2002. 11 - Glaciolacustrine environments, in: Menzies, J. (Ed.), Modern and
889 Past Glacial Environments. Butterworth-Heinemann, Oxford, pp. 335–359.
890 <https://doi.org/10.1016/B978-075064226-2/50014-3>

891 Ayalew, D., Jung, S., Romer, R.L., Kersten, F., Pfänder, J.A., Garbe-Schönberg, D., 2016.
892 Petrogenesis and origin of modern Ethiopian rift basalts: Constraints from isotope
893 and trace element geochemistry. Lithos 258–259, 1–14.
894 <https://doi.org/10.1016/j.lithos.2016.04.001>

895 Bajard, M., Poulénard, J., Sabatier, P., Develle, A.-L., Giguët-Covex, C., Jacob, J., Crouzet, C.,
896 David, F., Pignol, C., Arnaud, F., 2017. Progressive and regressive soil evolution
897 phases in the Anthropocene. CATENA 150, 39–52.
898 <https://doi.org/10.1016/j.catena.2016.11.001>

899 Bajard, M., Sabatier, P., David, F., Develle, A.-L., Reyss, J.-L., Fanget, B., Malet, E., Arnaud, D.,
900 Augustin, L., Crouzet, C., Poulénard, J., Arnaud, F., 2016. Erosion record in Lake La
901 Thuile sediments (Prealps, France): Evidence of montane landscape dynamics
902 throughout the Holocene. The Holocene 26, 350–364.
903 <https://doi.org/10.1177/0959683615609750>

904 Barberi, F., Varet, J., 1977. Volcanism of Afar: Small-scale plate tectonics implications. Geol.
905 Soc. Am. Bull., 88, 1251–1266.

906 Bastian, L., Vigier, N., Revel, M., Yirgu, G., Ayalew, D., Pik, R., 2019. Chemical erosion rates in
907 the upper Blue Nile Basin and related atmospheric CO₂ consumption. Chemical
908 Geology 518, 19–31. <https://doi.org/10.1016/j.chemgeo.2019.03.033>

909 Bates, C.C., 1953. RATIONAL THEORY OF DELTA FORMATION1. AAPG Bulletin 37, 2119–2162.
910 <https://doi.org/10.1306/5CEADD76-16BB-11D7-8645000102C1865D>

911 Beck, H.E., Wood, E.F., Pan, M., Fisher, C.K., Miralles, D.G., Dijk, A.I.J.M. van, McVicar, T.R.,
912 Adler, R.F., 2019. MSWEP V2 Global 3-Hourly 0.1° Precipitation: Methodology and
913 Quantitative Assessment. Bulletin of the American Meteorological Society 100, 473–
914 500. <https://doi.org/10.1175/BAMS-D-17-0138.1>

915 Bertin, X., Chaumillon, E., 2005. New Insights in Shallow Gas Generation from Very High
916 Resolution Seismic and Bathymetric Surveys in the Marennes-Oléron Bay, France.
917 Mar Geophys Res 26, 225–233. <https://doi.org/10.1007/s11001-005-3720-y>

918 Borton, J., 1997. Ethiopia Monthly Information Report Apr 1997. United Nations
919 Emergencies Unit for Ethiopia (UN-EUE).

920 Borton, J., 7. Ethiopia Monthly Information Report March 1997. United Nations Emergencies
921 Unit for Ethiopia.

922 Brown, M.C., Hervé, G., Korte, M., Genevey, A., 2021. Global archaeomagnetic data: The
923 state of the art and future challenges. Physics of the Earth and Planetary Interiors
924 318, 106766. <https://doi.org/10.1016/j.pepi.2021.106766>

925 Bruel, R., Sabatier, P., 2020. serac: an R package for Shortlived RADionuclide chronology of
926 recent sediment cores. Journal of Environmental Radioactivity 225, 106449.
927 <https://doi.org/10.1016/j.jenvrad.2020.106449>

928 Cai, W., Ng, B., Geng, T., Jia, F., Wu, L., Wang, G., Liu, Yu, Gan, B., Yang, K., Santoso, A., Lin,
929 X., Li, Z., Liu, Yi, Yang, Y., Jin, F.-F., Collins, M., McPhaden, M.J., 2023. Anthropogenic

930 impacts on twentieth-century ENSO variability changes. *Nat Rev Earth Environ* 1–12.
931 <https://doi.org/10.1038/s43017-023-00427-8>

932 Camberlin, P., Janicot, S., Pocard, I., 2001. Seasonality and atmospheric dynamics of the
933 teleconnection between African rainfall and tropical sea-surface temperature:
934 Atlantic vs. ENSO. *International Journal of Climatology* 21, 973–1005.
935 <https://doi.org/10.1002/joc.673>

936 Campbell, C., 1998. Late Holocene Lake Sedimentology and Climate Change in Southern
937 Alberta, Canada. *Quaternary Research* 49, 96–101.
938 <https://doi.org/10.1006/qres.1997.1946>

939 Campos, H., Steffen, W., Agüero, G., Parra, O., Zuniga, L., 1989. Estudios limnológicos en el
940 Lago Puyehue (Chile) : morfometría, factores físicos y químicos, plancton y
941 productividad primaria. *Medio ambiente (Valdivia)* 10, 36–53.

942 Campuzano, S.A., Gómez-Paccard, M., Pavón-Carrasco, F.J., Osete, M.L., 2019. Emergence
943 and evolution of the South Atlantic Anomaly revealed by the new paleomagnetic
944 reconstruction SHAWQ2k. *Earth and Planetary Science Letters* 512, 17–26.
945 <https://doi.org/10.1016/j.epsl.2019.01.050>

946 CARE, 1998. El Niño in 1997-1998: Impacts and CARE's Response.

947 Chapron, E., Ariztegui, D., Mulsow, S., Villarosa, G., Pino, M., Outes, V., Juvignié, E., Crivelli,
948 E., 2006. Impact of the 1960 major subduction earthquake in Northern Patagonia
949 (Chile, Argentina). *Quaternary International, Holocene environmental catastrophes in*
950 *South America: from the lowlands to the Andes* 158, 58–71.
951 <https://doi.org/10.1016/j.quaint.2006.05.017>

952 Chapron, E., Juvigné, E., Mulsow, S., Ariztegui, D., Magand, O., Bertrand, S., Pino, M.,
953 Chapron, O., 2007. Recent clastic sedimentation processes in Lake Puyehue (Chilean
954 Lake District, 40.5°S). *Sedimentary Geology* 201, 365–385.
955 <https://doi.org/10.1016/j.sedgeo.2007.07.006>

956 Cohen, A.S., 2003. *Paleolimnology: The History and Evolution of Lake Systems*. Oxford
957 University Press.

958 Comenetz, J., Caviedes, C., 2002. Climate variability, political crises, and historical population
959 displacements in Ethiopia. *Global Environmental Change Part B: Environmental*
960 *Hazards* 4, 113–127. <https://doi.org/10.1016/j.hazards.2003.08.001>

961 Coron, L., Delaigue, O., Thirel, G., Dorchie, D., Perrin, C., Michel, C., 2022. airGR: Suite of GR
962 Hydrological Models for Precipitation-Runoff Modelling (v. 1.7.0). airGR.

963 Coron, L., Thirel, G., Delaigue, O., Perrin, C., Andréassian, V., 2017. The suite of lumped GR
964 hydrological models in an R package. *Environmental Modelling & Software* 94, 166–
965 171. <https://doi.org/10.1016/j.envsoft.2017.05.002>

966 Croudace, I.W., Rothwell, R.G. (Eds.), 2015. *Micro-XRF Studies of Sediment Cores,*
967 *Developments in Paleoenvironmental Research*. Springer Netherlands, Dordrecht.
968 <https://doi.org/10.1007/978-94-017-9849-5>

969 Crouzet, C., Wilhelm, B., Sabatier, P., Demory, F., Thouveny, N., Pignol, C., Reyss, J.-L.,
970 Magand, O., Jeltsch-Thömmes, A., Bajard, M., Augustin, L., Arnaud, F., 2019.
971 Palaeomagnetism for chronologies of recent alpine lake sediments: successes and
972 limits. *J Paleolimnol* 62, 259–278. <https://doi.org/10.1007/s10933-019-00087-z>

973 De Putter, T., Loutre, M.-F., Wansard, G., 1998. Decadal periodicities of Nile River historical
974 discharge (A.D. 622–1470) and climatic implications. *Geophysical Research Letters*
975 25, 3193–3196. <https://doi.org/10.1029/98GL02250>

- 976 Dereje, H., Daneal, S.F., Yenesew, M., Azage, G.Y., Tadesse, S., Naod, M., Tariku, A., 2018.
 977 The Study of Water Use and Treated Wastewater Discharge charge. Report on Charge
 978 System for Irrigation Water Abstraction and Use. Federal Democratic Republic of
 979 Ethiopia Awash Basin Authority.
- 980 Dosio, A., Jones, R.G., Jack, C., Lennard, C., Nikulin, G., Hewitson, B., 2019. What can we
 981 know about future precipitation in Africa? Robustness, significance and added value
 982 of projections from a large ensemble of regional climate models. *Clim Dyn* 53, 5833–
 983 5858. <https://doi.org/10.1007/s00382-019-04900-3>
- 984 Eltahir, E.A.B., 1996. El Niño and the Natural Variability in the Flow of the Nile River. *Water*
 985 *Resour. Res.* 32, 131–137. <https://doi.org/10.1029/95WR02968>
- 986 Emerton, R., Cloke, H.L., Stephens, E.M., Zsoter, E., Woolnough, S.J., Pappenberger, F., 2017.
 987 Complex picture for likelihood of ENSO-driven flood hazard. *Nat Commun* 8, 14796.
 988 <https://doi.org/10.1038/ncomms14796>
- 989 FAO, 2023. Drought in the Horn of Africa: Progress report on the rapid response and
 990 mitigation plan to avert a humanitarian catastrophe (January–December 2022). FAO.
 991 <https://doi.org/10.4060/cc4218en>
- 992 FAO, 2022. Drought in the Horn of Africa – Rapid response and mitigation plan to avert a
 993 humanitarian catastrophe. FAO. <https://doi.org/10.4060/cb8280en>
- 994 FAO, 2000. The Elimination of Food Insecurity in the Horn of Africa – Summary Report.
 995 Rome.
- 996 Ficchi, A., Cloke, H., Neves, C., Woolnough, S., Coughlan de Perez, E., Zsoter, E., Pinto, I.,
 997 Meque, A., Stephens, E., 2021. Beyond El Niño: Unsung climate modes drive African
 998 floods. *Weather and Climate Extremes* 33, 100345.
 999 <https://doi.org/10.1016/j.wace.2021.100345>
- 1000 Folk, R.L., Ward, W.C., 1957. Brazos River Bar: A Study in the Significance of Grain Size
 1001 Parameters. *Journal Of Sedimentary Petrology* 27, 3–26.
- 1002 Fontaine, R.E., Najjar, A.E., Prince, J.S., 1961. The 1958 malaria epidemic in Ethiopia. *Am J*
 1003 *Trop Med Hyg* 10, 795–803. <https://doi.org/10.4269/ajtmh.1961.10.795>
- 1004 Foucher, A., Chaboche, P.-A., Sabatier, P., Evrard, O., 2021. A worldwide meta-analysis
 1005 (1977–2020) of sediment core dating using fallout radionuclides including ¹³⁷Cs and
 1006 ²¹⁰Pb_{xs}. *Earth System Science Data* 13, 4951–4966. <https://doi.org/10.5194/essd-13-4951-2021>
- 1007
- 1008 FSNAU, 2022. Somalia FSNAU Food Security & Nutrition Quarterly Brief — Focus on Post Gu
 1009 2017 Season Early Warning (Food Security and Nutrition Analysis Unit and Famine
 1010 Early Warning System Network, 2022). FSNAU.
- 1011 Garcia-Gil, S., Vilas, F., Garcia-Garcia, A., 2002. Shallow gas features in incised-valley fills (Ría
 1012 de Vigo, NW Spain): a case study. *Continental Shelf Research* 22, 2303–2315.
 1013 [https://doi.org/10.1016/S0278-4343\(02\)00057-2](https://doi.org/10.1016/S0278-4343(02)00057-2)
- 1014 Gilli, A., Anselmetti, F.S., Glur, L., Wirth, S.B., 2013. Lake Sediments as Archives of
 1015 Recurrence Rates and Intensities of Past Flood Events, in: Schneuwly-Bollschweiler,
 1016 M., Stoffel, M., Rudolf-Miklau, F. (Eds.), *Dating Torrential Processes on Fans and*
 1017 *Cones: Methods and Their Application for Hazard and Risk Assessment, Advances in*
 1018 *Global Change Research*. Springer Netherlands, Dordrecht, pp. 225–242.
 1019 https://doi.org/10.1007/978-94-007-4336-6_15
- 1020 Grothe, P.R., Cobb, K.M., Liguori, G., Di Lorenzo, E., Capotondi, A., Lu, Y., Cheng, H., Edwards,
 1021 R.L., Southon, J.R., Santos, G.M., Deocampo, D.M., Lynch-Stieglitz, J., Chen, T., Sayani,
 1022 H.R., Thompson, D.M., Conroy, J.L., Moore, A.L., Townsend, K., Hagos, M., O’Connor,

1023 G., Toth, L.T., 2020. Enhanced El Niño–Southern Oscillation Variability in Recent
1024 Decades. *Geophysical Research Letters* 47, e2019GL083906.
1025 <https://doi.org/10.1029/2019GL083906>

1026 Habertzettl, T., Kirsten, K.L., Kasper, T., Franz, S., Reinwarth, B., Baade, J., Daut, G., Meadows,
1027 M.E., Su, Y., Mäusbacher, R., 2019. Using 210Pb-data and paleomagnetic secular
1028 variations to date anthropogenic impact on a lake system in the Western Cape, South
1029 Africa. *Quaternary Geochronology* 51, 53–63.
1030 <https://doi.org/10.1016/j.quageo.2018.12.004>

1031 Hersbach, H., Bell, B., Berrisford, P., Hirahara, S., Horányi, A., Muñoz-Sabater, J., Nicolas, J.,
1032 Peubey, C., Radu, R., Schepers, D., Simmons, A., Soci, C., Abdalla, S., Abellan, X.,
1033 Balsamo, G., Bechtold, P., Biavati, G., Bidlot, J., Bonavita, M., De Chiara, G., Dahlgren,
1034 P., Dee, D., Diamantakis, M., Dragani, R., Flemming, J., Forbes, R., Fuentes, M., Geer,
1035 A., Haimberger, L., Healy, S., Hogan, R.J., Hólm, E., Janisková, M., Keeley, S., Laloyaux,
1036 P., Lopez, P., Lupu, C., Radnoti, G., de Rosnay, P., Rozum, I., Vamborg, F., Villaume, S.,
1037 Thépaut, J.-N., 2020. The ERA5 global reanalysis. *Quarterly Journal of the Royal
1038 Meteorological Society* 146, 1999–2049. <https://doi.org/10.1002/qj.3803>

1039 Hua, Q., Barbetti, M., Rakowski, A.Z., 2013. Atmospheric radiocarbon for the period 1950-
1040 2010.

1041 IPCC, 2022. Working Group II contribution to the Sixth Assessment Report of the
1042 Intergovernmental Panel on Climate Change.

1043 Jackson, A., Jonkers, A.R.T., Walker, M.R., 2000. Four Centuries of Geomagnetic Secular
1044 Variation from Historical Records. *Philosophical Transactions: Mathematical, Physical
1045 and Engineering Sciences* 358, 957–990.

1046 Jackson, M.L., 2005. Soil chemical analysis : advanced course : a manual of methods useful
1047 for instruction and research in soil chemistry, physical chemistry of soils, soil fertility,
1048 and soil genesis. Parallel Press, University of Wisconsin-Madison Libraries, [2005]
1049 ©2005, Revised second edition. Madison, Wis.

1050 Jenny, J.-P., Wilhelm, B., Arnaud, F., Sabatier, P., Giguet Covex, C., Mélo, A., Fanget, B.,
1051 Malet, E., Ployon, E., Perga, M.E., 2014. A 4D sedimentological approach to
1052 reconstructing the flood frequency and intensity of the Rhône River (Lake Bourget,
1053 NW European Alps). *J Paleolimnol* 51, 469–483. <https://doi.org/10.1007/s10933-014-9768-4>

1054

1055 Kidane, D., Mekonnen, A., Teketay, D., 2014. Contributions of Tendaho Irrigation Project to
1056 the Improvement of Livelihoods of Agropastoralists in the Lower Awash Basin,
1057 Northeastern Ethiopia. *Ethiopian e-journal for research and innovation foresight* 6, 1–
1058 19.

1059 Kylander, M.E., Ampel, L., Wohlfarth, B., Veres, D., 2011. High-resolution X-ray fluorescence
1060 core scanning analysis of Les Echets (France) sedimentary sequence: new insights
1061 from chemical proxies. *Journal of Quaternary Science* 26, 109–117.
1062 <https://doi.org/10.1002/jqs.1438>

1063 Lapointe, F., Francus, P., Lamoureux, S.F., Saïd, M., Cuvén, S., 2012. 1750 years of large
1064 rainfall events inferred from particle size at East Lake, Cape Bounty, Melville Island,
1065 Canada. *J Paleolimnol* 48, 159–173. <https://doi.org/10.1007/s10933-012-9611-8>

1066 Lefebvre, P., Sabatier, P., Mangeret, A., Gourgiotis, A., Le Pape, P., Develle, A.-L., Louvat, P.,
1067 Diez, O., Reyss, J.-L., Gaillardet, J., Cazala, C., Morin, G., 2021. Climate-driven fluxes of
1068 organic-bound uranium to an alpine lake over the Holocene. *Science of The Total
1069 Environment* 783, 146878. <https://doi.org/10.1016/j.scitotenv.2021.146878>

- 1070 Lennard, C.J., Nikulin, G., Dosio, A., Moufouma-Okia, W., 2018. On the need for regional
1071 climate information over Africa under varying levels of global warming. *Environ. Res.*
1072 *Let.* 13, 060401. <https://doi.org/10.1088/1748-9326/aab2b4>
- 1073 Li, C.-G., Zheng, Y., Wang, M., Sun, Z., Jin, C., Hou, J., 2021. Refined dating using
1074 palaeomagnetic secular variations on a lake sediment core from Guozha Co,
1075 northwestern Tibetan Plateau. *Quaternary Geochronology* 62, 101146.
1076 <https://doi.org/10.1016/j.quageo.2020.101146>
- 1077 MacLeod, D., Caminade, C., 2019. The Moderate Impact of the 2015 El Niño over East Africa
1078 and Its Representation in Seasonal Reforecasts. *Journal of Climate* 32, 7989–8001.
1079 <https://doi.org/10.1175/JCLI-D-19-0201.1>
- 1080 Martín-Puertas, C., Valero-Garcés, B.L., Mata, M.P., Moreno, A., Giralte, S., Martínez-Ruiz, F.,
1081 Jiménez-Espejo, F., 2011. Geochemical processes in a Mediterranean Lake: a high-
1082 resolution study of the last 4,000 years in Zoñar Lake, southern Spain. *Journal of*
1083 *Paleolimnology* 46, 405–421. <https://doi.org/10.1007/s10933-009-9373-0>
- 1084 Marzin, C., Braconnot, P., 2009. The role of the ocean feedback on Asian and African
1085 monsoon variations at 6kyr and 9.5kyr BP. *Comptes Rendus Geoscience* 341, 643–
1086 655. <https://doi.org/10.1016/j.crte.2009.09.001>
- 1087 Mera, G.A., 2018. Drought and its impacts in Ethiopia. *Weather and Climate Extremes* 22,
1088 24–35. <https://doi.org/10.1016/j.wace.2018.10.002>
- 1089 Molinaroli, E., Guerzoni, S., De Falco, G., Sarretta, A., Cucco, A., Como, S., Simeone, S., Perilli,
1090 A., Magni, P., 2009. Relationships between hydrodynamic parameters and grain size
1091 in two contrasting transitional environments: The Lagoons of Venice and Cabras,
1092 Italy. *Sedimentary Geology* 219, 196–207.
1093 <https://doi.org/10.1016/j.sedgeo.2009.05.013>
- 1094 Mologni, C., Bruxelles, L., Schuster, M., Davtian, G., Ménard, C., Orange, F., Doubre, C.,
1095 Cauliez, J., Tazaz, H.B., Revel, M., Khalidi, L., 2021. Holocene East African monsoonal
1096 variations recorded in wave-dominated clastic paleo-shorelines of Lake Abhe, Central
1097 Afar region (Ethiopia & Djibouti). *Geomorphology* 391, 107896.
1098 <https://doi.org/10.1016/j.geomorph.2021.107896>
- 1099 Mologni, C., Revel, M., Blanchet, C., Bosch, D., Develle, A.-L., Orange, F., Bastian, L., Khalidi,
1100 L., Ducassou, E., Migeon, S., 2020. Frequency of exceptional Nile flood events as an
1101 indicator of Holocene hydro-climatic changes in the Ethiopian Highlands. *Quaternary*
1102 *Science Reviews* 247, 106543. <https://doi.org/10.1016/j.quascirev.2020.106543>
- 1103 Mouelhi, S., Michel, C., Perrin, C., Andréassian, V., 2006. Stepwise development of a two-
1104 parameter monthly water balance model. *Journal of Hydrology* 318, 200–214.
1105 <https://doi.org/10.1016/j.jhydrol.2005.06.014>
- 1106 Murray, H.D., 1975. *Melanoides tuberculata* (Müller), Las Morras Creek, Bracketville.
1107 *Bulletin Of The American Malacological Union* 1, 43.
- 1108 Nash, J.E., Sutcliffe, J.V., 1970. River flow forecasting through conceptual models part I — A
1109 discussion of principles. *Journal of Hydrology* 10, 282–290.
1110 [https://doi.org/10.1016/0022-1694\(70\)90255-6](https://doi.org/10.1016/0022-1694(70)90255-6)
- 1111 Niang, I., Ruppel, O.C., Abdrabo, M.A., Essel, A., Lennard, C., Padgham, J., Urquhart, P.,
1112 Adelekan, I., Archibald, S., Barkhordarian, A., Battersby, J., Chahed, M., Chatterjee,
1113 M., Chidzie, C.T., Descheemaeker, K., Djoudi, H., Ebi, K.L., Fall, P.D., Fuentes, R.,
1114 Garland, R., Harvey, B., Hayden, M., Hemp, A., Jobbins, G., Johnson, J., Lobell, D.,
1115 Locatelli, B., Ludi, E., Naess, L.O., Ndebele-Murisa, M.R., Ndiaye, A., Newsham, A.,
1116 Njai, S., Pauw, P., Pramova, E., Rakotondrafara, M.-L., Raleigh, C., Roberts, D.,

1117 Schleyer, M.H., Victor, D., Vincent, K., Dube, P., Leary, N., Schulte-Uebbing, L., 2014.
 1118 Part B: Regional Aspects. Contribution of Working Group II to the Fifth Assessment
 1119 Report of the Intergovernmental Panel on Climate Change - Africa, in: Climate
 1120 Change 2014: Impacts, Adaptation, and Vulnerability., Cambridge University Press.
 1121 Cambridge, United Kingdom and New York, NY, USA, pp. 1199–1265.
 1122 Nicholson, S.E., 2017. Climate and climatic variability of rainfall over eastern Africa. *Reviews*
 1123 *of Geophysics* 55, 590–635. <https://doi.org/10.1002/2016RG000544>
 1124 OCHA, 2022. Horn of Africa Drought: Regional Humanitarian Overview & Call to Action.
 1125 OCHA.
 1126 Ólafsdóttir, S., Geirsdóttir, Á., Miller, G.H., Stoner, J.S., Channell, J.E.T., 2013. Synchronizing
 1127 Holocene lacustrine and marine sediment records using paleomagnetic secular
 1128 variation. *Geology* 41, 535–538. <https://doi.org/10.1130/G33946.1>
 1129 Oudin, L., Hervieu, F., Michel, C., Perrin, C., Andréassian, V., Anctil, F., Loumagne, C., 2005.
 1130 Which potential evapotranspiration input for a lumped rainfall–runoff model?: Part
 1131 2—Towards a simple and efficient potential evapotranspiration model for rainfall–
 1132 runoff modelling. *Journal of Hydrology* 303, 290–306.
 1133 <https://doi.org/10.1016/j.jhydrol.2004.08.026>
 1134 Palmer, P.I., Wainwright, C.M., Dong, B., Maidment, R.I., Wheeler, K.G., Gedney, N.,
 1135 Hickman, J.E., Madani, N., Folwell, S.S., Abdo, G., Allan, R.P., Black, E.C.L., Feng, L.,
 1136 Gudoshava, M., Haines, K., Huntingford, C., Kilavi, M., Lunt, M.F., Shaaban, A., Turner,
 1137 A.G., 2023. Drivers and impacts of Eastern African rainfall variability. *Nat Rev Earth*
 1138 *Environ* 4, 254–270. <https://doi.org/10.1038/s43017-023-00397-x>
 1139 Parris, A.S., Bierman, P.R., Noren, A.J., Prins, M.A., Lini, A., 2010. Holocene paleostorms
 1140 identified by particle size signatures in lake sediments from the northeastern United
 1141 States. *J Paleolimnol* 43, 29–49. <https://doi.org/10.1007/s10933-009-9311-1>
 1142 Pekel, J.-F., Cottam, A., Gorelick, N., Belward, A.S., 2016. High-resolution mapping of global
 1143 surface water and its long-term changes. *Nature* 540, 418–422.
 1144 <https://doi.org/10.1038/nature20584>
 1145 Phillips, J.D., 2003. Sources of nonlinearity and complexity in geomorphic systems. *Progress*
 1146 *in Physical Geography: Earth and Environment* 27, 1–23.
 1147 <https://doi.org/10.1191/0309133303pp340ra>
 1148 Rauch, S., Hemond, H.F., Brabander, D.J., 2006. High spatial resolution analysis of lake
 1149 sediment cores by laser ablation inductively coupled plasma-mass spectrometry (LA-
 1150 ICP-MS): Lake sediment cores by laser ablation-ICP-MS. *Limnol. Oceanogr. Methods*
 1151 4, 268–274. <https://doi.org/10.4319/lom.2006.4.268>
 1152 Reyss, J.-L., Schmidt, S., Legeleux, F., Bonté, P., 1995. Large, low background well-type
 1153 detectors for measurements of environmental radioactivity. *Nuclear Instruments and*
 1154 *Methods in Physics Research Section A: Accelerators, Spectrometers, Detectors and*
 1155 *Associated Equipment* 357, 391–397. [https://doi.org/10.1016/0168-9002\(95\)00021-6](https://doi.org/10.1016/0168-9002(95)00021-6)
 1156 Roussel, E.G., Sauvadet, A.-L., Allard, J., Chaduteau, C., Richard, P., Bonavita, M.-A.C.,
 1157 Chaumillon, E., 2009. Archaeal Methane Cycling Communities Associated with Gassy
 1158 Subsurface Sediments of Marennes-Oléron Bay (France). *Geomicrobiology Journal*
 1159 26, 31–43. <https://doi.org/10.1080/01490450802599284>
 1160 Sabatier, P., Moernaut, J., Bertrand, S., Van Daele, M., Kremer, K., Chaumillon, E., Arnaud, F.,
 1161 2022. A Review of Event Deposits in Lake Sediments. *Quaternary* 5, 34.
 1162 <https://doi.org/10.3390/quat5030034>

1163 Sabatier, P., Wilhelm, B., Ficetola, G.F., Moiroux, F., Poulenard, J., Develle, A.-L., Bichet, A.,
1164 Chen, W., Pignol, C., Reyss, J.-L., Gielly, L., Bajard, M., Perrette, Y., Malet, E., Taberlet,
1165 P., Arnaud, F., 2017. 6-kyr record of flood frequency and intensity in the western
1166 Mediterranean Alps – Interplay of solar and temperature forcing. *Quaternary Science*
1167 *Reviews* 170, 121–135. <https://doi.org/10.1016/j.quascirev.2017.06.019>

1168 Schiefer, E., Gilbert, R., Hassan, M.A., 2011. A lake sediment-based proxy of floods in the
1169 Rocky Mountain Front Ranges, Canada. *J Paleolimnol* 45, 137–149.
1170 <https://doi.org/10.1007/s10933-010-9485-6>

1171 Slivinski, L.C., Compo, G.P., Whitaker, J.S., Sardeshmukh, P.D., Giese, B.S., McColl, C., Allan,
1172 R., Yin, X., Vose, R., Titchner, H., Kennedy, J., Spencer, L.J., Ashcroft, L., Brönnimann,
1173 S., Brunet, M., Camuffo, D., Cornes, R., Cram, T.A., Crouthamel, R., Domínguez-
1174 Castro, F., Freeman, J.E., Gergis, J., Hawkins, E., Jones, P.D., Jourdain, S., Kaplan, A.,
1175 Kubota, H., Blancq, F.L., Lee, T.-C., Lorrey, A., Luterbacher, J., Maugeri, M., Mock, C.J.,
1176 Moore, G.W.K., Przybylak, R., Pudmenzky, C., Reason, C., Slonosky, V.C., Smith, C.A.,
1177 Tinz, B., Trewin, B., Valente, M.A., Wang, X.L., Wilkinson, C., Wood, K., Wyszyński, P.,
1178 2019. Towards a more reliable historical reanalysis: Improvements for version 3 of
1179 the Twentieth Century Reanalysis system. *Quarterly Journal of the Royal*
1180 *Meteorological Society* 145, 2876–2908. <https://doi.org/10.1002/qj.3598>

1181 Spencer, T., Laughton, A.S., Flemming, N.C., Black, E., 2005. The relationship between Indian
1182 Ocean sea–surface temperature and East African rainfall. *Philosophical Transactions*
1183 *of the Royal Society A: Mathematical, Physical and Engineering Sciences* 363, 43–47.
1184 <https://doi.org/10.1098/rsta.2004.1474>

1185 Syvitski, J., Ángel, J.R., Saito, Y., Overeem, I., Vörösmarty, C.J., Wang, H., Olago, D., 2022.
1186 Earth’s sediment cycle during the Anthropocene. *Nat Rev Earth Environ* 3, 179–196.
1187 <https://doi.org/10.1038/s43017-021-00253-w>

1188 Taddese, G., Sonder, K., Peden, D., 2010. THE WATER OF THE AWASH RIVER BASIN A FUTURE
1189 CHALLENGE TO ETHIOPIA. report 14.

1190 Varet, J., 2018. *Geology of Afar (East Africa)*, Springer. ed, *Regional Geology Reviews*.

1191 Wang, G., Eltahir, E.A.B., 1999. Use of ENSO Information in Medium- and Long-Range
1192 Forecasting of the Nile Floods. *Journal of Climate* 12, 1726–1737.
1193 [https://doi.org/10.1175/1520-0442\(1999\)012<1726:UOEIIM>2.0.CO;2](https://doi.org/10.1175/1520-0442(1999)012<1726:UOEIIM>2.0.CO;2)

1194 Ward, P.J., Eisner, S., Flörke, M., Dettinger, M.D., Kummerow, M., 2014. Annual flood
1195 sensitivities to El Niño–Southern Oscillation at the global scale. *Hydrology and Earth*
1196 *System Sciences* 18, 47–66. <https://doi.org/10.5194/hess-18-47-2014>

1197 WBG, 2018. *Somalia Drought Impact and Needs Assessment: Synthesis Report* (World Bank
1198 Group, 2018). World Bank Group.

1199 Webster, P.J., Moore, A.M., Loschnigg, J.P., Leben, R.R., 1999. Coupled ocean-atmosphere
1200 dynamics in the Indian Ocean during 1997-98. *Nature* 401, 356–360.
1201 <https://doi.org/10.1038/43848>

1202 Weltje, G.J., Tjallingii, R., 2008. Calibration of XRF core scanners for quantitative geochemical
1203 logging of sediment cores: Theory and application. *Earth and Planetary Science*
1204 *Letters* 274, 423–438. <https://doi.org/10.1016/j.epsl.2008.07.054>

1205 Wilhelm, B., Arnaud, F., Sabatier, P., Crouzet, C., Brisset, E., Guiter, F., Reyss, J.L., Chaumillon,
1206 E., Tachikawa, K., Bard, E., Delannoy, J.J., 2012. 1.4 kyrs of flash flood events in the
1207 Southern European Alps: implications for extreme precipitation patterns and forcing
1208 over the north-western Mediterranean area 9097.

- 1209 Wilhelm, B., Ballesteros Canovas, J.A., Corella Aznar, J.P., Kämpf, L., Swierczynski, T., Stoffel,
1210 M., Støren, E., Toonen, W., 2018. Recent advances in paleoflood hydrology: From
1211 new archives to data compilation and analysis. *Water Security* 3, 1–8.
1212 <https://doi.org/10.1016/j.wasec.2018.07.001>
- 1213 Wilhelm, B., Rapuc, W., Amann, B., Anselmetti, F.S., Arnaud, F., Blanchet, J., Brauer, A.,
1214 Czymzik, M., Giguet-Covex, C., Gilli, A., Glur, L., Grosjean, M., Irmler, R., Nicolle, M.,
1215 Sabatier, P., Swierczynski, T., Wirth, S.B., 2022. Impact of warmer climate periods on
1216 flood hazard in the European Alps. *Nat. Geosci.* 15, 118–123.
1217 <https://doi.org/10.1038/s41561-021-00878-y>
- 1218 Wilhelm, B., Sabatier, P., Arnaud, F., 2015. Is a regional flood signal reproducible from lake
1219 sediments? *Sedimentology* 62, 1103–1117. <https://doi.org/10.1111/sed.12180>
- 1220 Yemane, W., 2008. Challenges and Prospects of Commercial Agriculture Enterprise
1221 Development and the Afar Pastoralists: The Case of Tendaho Dam and Irrigation
1222 Project. Addis Ababa University, Addis Ababa.
- 1223 Zaroug, M.A.H., Eltahir, E.A.B., Giorgi, F., 2014. Droughts and floods over the upper
1224 catchment of the Blue Nile and their connections to the timing of El Niño and La Niña
1225 events. *Hydrol. Earth Syst. Sci.* 18, 1239–1249. [https://doi.org/10.5194/hess-18-](https://doi.org/10.5194/hess-18-1239-2014)
1226 [1239-2014](https://doi.org/10.5194/hess-18-1239-2014)
1227
1228